

Technical note: Gas-phase nitrate radical generation via irradiation of aerated ceric ammonium nitrate mixtures

Andrew T. Lambe¹, Bin Bai², Masayuki Takeuchi³, Nicole Orwat⁴, Paul M. Zimmerman⁴, Mitchell W. Alton¹, Nga L. Ng^{2,3,5}, Andrew Freedman¹, Megan S. Clafin¹, Drew R. Gentner^{6,7}, Douglas R. Worsnop¹, and Pengfei Liu²

¹Aerodyne Research, Inc., Billerica, MA, USA

²School of Earth and Atmospheric Sciences, Georgia Institute of Technology, Atlanta, GA, USA

³School of Civil and Environmental Engineering, Georgia Institute of Technology, Atlanta, GA, USA

⁴Department of Chemistry, University of Michigan, Ann Arbor, MI, USA

⁵School of Chemical and Biomolecular Engineering, Georgia Institute of Technology, Atlanta, GA, USA

⁶Department of Chemical and Environmental Engineering, Yale University, New Haven, CT, USA

⁷School of the Environment, Yale University, New Haven, CT, USA

Correspondence: Andrew T. Lambe (lambe@aerodyne.com)

Abstract.

We present a novel photolytic source of gas-phase NO_3 suitable for use in atmospheric chemistry studies that has several advantages over traditional sources that utilize $\text{NO}_2 + \text{O}_3$ reactions and/or thermal dissociation of dinitrogen pentoxide (N_2O_5). The method generates NO_3 via irradiation of aerated aqueous solutions of ceric ammonium nitrate ($(\text{NH}_4)_2\text{Ce}(\text{NO}_3)_6$, “CAN”) and nitric acid (HNO_3) or sodium nitrate (NaNO_3). We present experimental and model characterization of the NO_3 formation potential of irradiated CAN/ HNO_3 and CAN/ NaNO_3 mixtures containing $[\text{CAN}] = 10^{-3}$ to 1.0 M, $[\text{HNO}_3] = 1.0$ to 6.0 M, $[\text{NaNO}_3] = 1.0$ to 4.8 M, photon fluxes (I) ranging from 6.9×10^{14} to 1.0×10^{16} photons $\text{cm}^{-2} \text{s}^{-1}$, and irradiation wavelengths ranging from 254 to 421 nm. NO_3 mixing ratios ranging from parts per billion to parts per million by volume were achieved using this method. At the CAN solubility limit, maximum $[\text{NO}_3]$ was achieved using $[\text{HNO}_3] \approx 3.0$ to 6.0 M and UVA radiation ($\lambda_{\text{max}} = 369$ nm) in CAN/ HNO_3 mixtures or $[\text{NaNO}_3] \geq 1.0$ M and UVC radiation ($\lambda_{\text{max}} = 254$ nm) in CAN/ NaNO_3 mixtures. Other reactive nitrogen (NO_2 , N_2O_4 , N_2O_5 , N_2O_6 , HNO_2 , HNO_3 , HNO_4) and reactive oxygen (HO_2 , H_2O_2) species obtained from the irradiation of ceric nitrate mixtures were measured using a NO_x analyzer and an iodide adduct high-resolution time-of-flight chemical ionization mass spectrometer (HR-ToF-CIMS). To assess the applicability of the method for studies of NO_3 -initiated oxidative aging processes, we generated and measured the chemical composition of oxygenated volatile organic compounds and secondary organic aerosols from the β -pinene + NO_3 reaction using a Filter Inlet for Gases and Aerosols (FIGAERO) coupled to the HR-ToF-CIMS.

1 Introduction

The importance of NO_3 as a nighttime atmospheric oxidant is well established (Wayne et al., 1991; Brown and Stutz, 2012; Ng et al., 2017; Wang et al., 2023). NO_3 is generated via the reaction $\text{NO}_2 + \text{O}_3 \rightarrow \text{NO}_3 + \text{O}_2$, followed by achievement of

20 temperature-dependent equilibrium between NO_3 , NO_2 , and dinitrogen pentoxide (N_2O_5). N_2O_5 also hydrolyzes efficiently to HNO_3 on aqueous surfaces (Brown et al., 2004). Thus, any investigation of the influence of NO_3 chemistry in a specific source region necessarily must account for the local temperature, humidity, and particle surface area along with other factors. Despite these complications, for decades, laboratory studies investigating gas-phase NO_3 chemistry have utilized the same $\text{NO}_2 + \text{O}_3$ reactions and/or N_2O_5 thermal decomposition to produce NO_3 as occurs in the atmosphere, and accommodated the
 25 inherent limitations associated with N_2O_5 ; namely, that it must be stored under cold and dry conditions until use. Few viable alternative methods for the generation of gas-phase NO_3 have been identified. Reactions between fluorine atoms and nitric acid ($\text{F} + \text{HNO}_3 \rightarrow \text{HF} + \text{NO}_3$), or chlorine atoms and chlorine nitrate ($\text{Cl} + \text{ClNO}_3 \rightarrow \text{Cl}_2 + \text{NO}_3$) require handling and/or synthesizing hazardous halogen-containing compounds (Burrows et al., 1985; Bedjanian, 2019). F and Cl can also compete with NO_3 for the oxidation of target analytes, as can O_3 if its reaction with NO_2 is used as the NO_3 source.

30 In the 1960s and 1970s, following earlier research into the properties of ceric solutions (Meyer and Jacoby, 1901; Wylie, 1951; Hinsvark and Stone, 1956; Blaustein and Gryder, 1957), Thomas Martin and coworkers discovered that irradiating solutions containing ceric ammonium nitrate (CAN, $(\text{NH}_4)_2\text{Ce}(\text{NO}_3)_6$) generates aqueous NO_3 (Henshall, 1963; Martin et al., 1963, 1964; Glass and Martin, 1970; Martin and Glass, 1970; Martin and Stevens, 1978). In $\gtrsim 6\text{M}$ nitric acid (HNO_3), CAN is thought to dissociate primarily into NH_4^+ cations and hexanitratocerate ($\text{Ce}(\text{NO}_3)_6^{2-}$) anions (Henshall, 1963). The
 35 $\text{Ce}(\text{NO}_3)_6^{2-}$ is subsequently reduced to $\text{Ce}(\text{NO}_3)_5^{2-}$ upon irradiation by ultraviolet light, and NO_3 is generated as a primary photolysis product. A similar process occurs in other solvents, although the ensuing ceric composition in solution is complex and influenced by several factors. For example, in glacial acetic acid (CH_3COOH), CAN dissociates into primarily $\text{Ce}(\text{NO}_3)_4$ (Henshall, 1963). Additionally, ceric ions containing complexed hydroxyl (OH) or H_2O , CH_3COOH , or acetonitrile (CH_3CN) molecules are formed in aqueous, acetic acid, or CH_3CN media, respectively (Henshall, 1963; Glebov et al., 2021). Higher
 40 solution acidity and/or CAN concentration appears to promote the formation of $\text{Ce}(\text{NO}_3)_6^{2-}$ (Wylie, 1951) and ceric nitrate dimers (Blaustein and Gryder, 1957; Demars et al., 2015). The following generalized mechanism was proposed by Glass and Martin (1970) to describe ceric nitrate photochemistry:



where $\text{Ce}^{(\text{IV})}$ represents ceric nitrates as diverse as $\text{Ce}(\text{NO}_3)_4$, $\text{Ce}(\text{NO}_3)_6^{2-}$, $(\text{NO}_3)_5\text{CeO}(\text{NO}_3)_5^{4-}$, and $(\text{H}_2\text{O})_3(\text{NO}_3)_3\text{CeO}(\text{NO}_3)_3(\text{H}_2\text{O})_3$ that are potentially formed in solution (Henshall, 1963; Blaustein and Gryder, 1957;
 50 Demars et al., 2015). Similarly, $\text{Ce}^{(\text{III})}$ represents cerous nitrates such as $\text{Ce}(\text{NO}_3)_3$ and $\text{Ce}(\text{NO}_3)_5^{2-}$. The rate of Reaction R2 is $[\text{HNO}_3]$ -dependent (Martin and Glass, 1970), and the dinitrogen hexaoxide (N_2O_6) intermediate was proposed on the basis of supporting observations without direct measurements (Glass and Martin, 1970).

CAN is used routinely as an oxidizing agent in organic synthesis due to its widespread availability and low cost, high oxidative potential, and low toxicity (Nair and Deepthi, 2007). However, its usage in atmospheric chemistry to date is limited to studies of NO₃-initiated oxidative aging processes in solution, e.g. Alexander (2004). Given the potential simplicity of irradiating Ce^(IV) mixtures relative to synthesizing and storing N₂O₅ under cold and dry conditions or reacting NO₂ + O₃ under carefully controlled conditions, Ce^(IV) irradiation could in principle enable more widespread studies of NO₃ oxidation chemistry, which is understudied compared to OH chemistry (Ng et al., 2017). Here, for the first time, we investigated the use of Ce^(IV) irradiation as a source of gas-phase NO₃. First, we designed a photoreactor that generates gas-phase NO₃ from irradiated CAN/HNO₃ and CAN/NaNO₃ mixtures. Second, we characterized NO₃ concentrations achieved over a range of reactor operating conditions and mixture composition. Third, we characterized gas-phase reactive nitrogen and reactive oxygen species generated following Ce^(IV) irradiation. Fourth, we demonstrated application of the method to generate and characterize OVOCs and SOA from the β-pinene + NO₃ reaction.

2 Methods

2.1 Photoreactor design and operation

Figure 1 shows a schematic of the experimental setup used in this study. A zero air carrier gas flow of 0.5 L min⁻¹ was bubbled through a gas dispersion line consisting of 6.35 mm OD x 4.8 mm ID FEP tubing into approximately 10 mL of aqueous CAN/HNO₃ or CAN/NaNO₃ mixtures placed at the bottom of a 12.7 mm OD x 11.1 cm ID FEP tube. The FEP tube was surrounded by low-pressure mercury fluorescent lamps installed vertically in a custom enclosure. These lamps had a 35.6 cm illuminated length. At these operating conditions, the calculated gas transit time in the illuminated portion of the reactor was approximately 3 s. After exiting the photoreactor, the carrier gas flow was passed through a filter holder (Savillex, 401-21-47-10-21-2) containing a 47 mm PTFE membrane filter (Pall Gelman, R2PJ047) to transmit NO₃ (Wagner et al., 2011) while removing stray droplets from the sample flow. At the end of each experiment, the lamps were turned off, the gas dispersion line was removed from the top of the reactor, and FEP tubing and filter holder were flushed with distilled H₂O to remove residual Ce^(III) precipitate. Initial studies were conducted using a Cavity Attenuated Phase Shift (CAPS) NO₂ monitor operating at λ = 405 nm (Kebabian et al., 2005) and a second retrofitted CAPS monitor operating at λ = 630 nm which established that NO₂ and NO₃ were produced from irradiated Ce^(IV). Subsequent studies described in the next section used a 2B Technologies Model 405 analyzer to measure NO and NO₂ (Birks et al., 2018).

Depending on the specific experiment, lamps with peak emission output centered at λ = 254, 313, 369, or 421 nm, respectively (GPH436TL/4P, Light Sources, Inc.; F436T5/NBUVB/4P-313, F436T5/BLC/4P-369, F436T5/SDI/4P-421, LCD Lighting, Inc.) were used. Emission spectra from the manufacturer are shown in Figure S1. A fluorescent dimming ballast (IZT-2S28-D, Advance Transformer Co.) was used to regulate current applied to the lamps. To quantify the photon flux \dot{I}_λ in the photoreactor for studies that used λ = 254, 313, or 369 nm radiation, we measured the rate of externally added O₃ (λ = 254 nm) or NO₂ photolysis (λ = 313 or 369 nm) as a function of lamp voltage under dry conditions (RH < 5%). The photon flux was not quantified in studies that used λ = 421 nm radiation. NO₂ photolysis measurements were conducted in the absence

of oxygen to avoid O₃ formation. I-values Photon flux values were then calculated using methods described in Lambe et al. (2019); maximum $I_{254} = 1.0 \times 10^{16}$ photons cm⁻² s⁻¹, $I_{313} = 6.0 \times 10^{15}$ photons cm⁻² s⁻¹, and $I_{369} = 7.0 \times 10^{15}$ photons cm⁻² s⁻¹ were obtained.

2.2 Characterization studies

90 In one set of experiments, the 0.5 L min⁻¹ photoreactor effluent was mixed with a 6.5 L min⁻¹ zero air carrier gas and injected into a dark Potential Aerosol Mass oxidation flow reactor (OFR; Aerodyne Research, Inc.), which is a horizontal 13 L Teflon-coated aluminum cylindrical chamber operated in continuous flow mode. Approximately 6.5 L min⁻¹ of sample flow was pulled from the reactor, resulting in a calculated mean residence time in the OFR (τ_{OFR}) of approximately 120 s. To constrain NO₃ mixing ratios, a mixture of 10 VOC tracers with NO₃ reaction rate coefficients (k_{NO_3}) ranging from 3.01×10^{-19} to
95 2.69×10^{-11} cm³ molecules⁻¹ s⁻¹ at $T = 298$ K (Table S1) was injected through a 10.2 cm length of 0.0152 cm ID Teflon tubing at a liquid flow rate of 0.94 $\mu\text{L hr}^{-1}$ using a syringe pump. The tracer mixture was then evaporated into a 1 L min⁻¹ zero air carrier gas prior to injection into the OFR. The total external NO₃ reactivity ($\text{NO}_3\text{R}_{\text{ext}}$), which is the summed product of each tracer mixing ratio and its k_{NO_3} , was approximately 5 s⁻¹. VOCs with proton affinities greater than that of H₂O were chosen to enable their measurement with a Tofwerk/Aerodyne Vocus proton transfer-reaction time-of-flight mass spectrometer
100 (hereafter referred to as “Vocus PTR”) operated using H₃O⁺ reagent ion chemistry (Krechmer et al., 2018) and ~ 8000 (Th/Th) resolving power. NO₃ mixing ratios were calculated from the measured decrease in VOC mixing ratios using the Vocus PTR. Here, we assumed that the total concentration of reacted VOCs was equal to the concentration of NO₃ injected into the OFR; ~~because~~. Because NO₃ may additionally react with organic peroxy radicals (RO₂) generated from VOC + NO₃ reactions as well as OVOCs, these calculated NO₃ concentrations represent lower limits. Modeling calculations suggest that the fractional
105 consumption of NO₃ by RO₂ ranged from <0.01 to 0.17 over the range of conditions that were studied (Fig. S2). A subset of OVOCs generated from VOC + NO₃ reactions that had proton affinities greater than that of H₂O were also detected with the Vocus PTR.

In a separate set of experiments, the photoreactor effluent was diluted into 4 L min⁻¹ zero air carrier gas and sampled with an Aerodyne iodide-adduct high-resolution time-of-flight chemical ionization mass spectrometer (HR-ToF-CIMS; hereafter
110 referred to as “CIMS”; Bertram et al. (2011)) and the NO_x analyzer. The CIMS was operated at a ~ 4000 (Th/Th) resolving power. Iodide-adduct reagent ion chemistry was used due to its high sensitivity and selectivity towards nitrogen oxides and multifunctional organic nitrates (Lee et al., 2014). To demonstrate application of the method to study NO₃-initiated oxidative aging processes, the chemical composition of β -pinene + NO₃ gas-and condensed-phase oxidation products was measured with a Filter Inlet for Gases and Aerosols (FIGAERO) coupled to the CIMS (Lopez-Hilfiker et al., 2013). Gas sampling and
115 simultaneous particle collection was performed for 1 min intervals, followed by thermal desorption of the particle sample from a PTFE filter membrane (15 min ramp from room temperature to 200°C, 10 min holding time, 8 min cooldown to room temperature).

2.3 Photochemical model

To supplement our measurements, and to characterize aqueous phase concentrations of species produced in the photoreactor that were not measured, we developed a photochemical box model that was implemented in the KinSim chemical kinetic solver (Peng and Jimenez, 2019). The KinSim mechanism shown in Table S2 contains 79 reactions to model concentrations of $\text{Ce}^{(\text{IV})}$, $\text{Ce}^{(\text{III})}$, NO , NO_2 , NO_3 , N_2O_3 , N_2O_4 , N_2O_5 , HNO_2 , HNO_3 , HNO_4 , H , O , OH , HO_2 , and H_2O_2 . We assumed that HNO_3 that was present in solution prior to irradiation completely dissociated into H^+ and NO_3^- . When possible, we used condensed-phase rate coefficients in the mechanism. For reactions that we assumed occurred but did not have published condensed-phase rate coefficients (e.g. $\text{NO}_3 + \text{OH} \rightarrow \text{NO}_2 + \text{HO}_2$) we used published gas-phase rate coefficients instead with no modifications aside from unit conversion. Gas-phase wall loss rates of NO_x , NO_y , and HO_x species were not explicitly considered in the mechanism. UV/Vis extinction cross sections (σ_{ext}) of CAN/ HNO_3 and CAN/ NaNO_3 mixtures were separately obtained between $\lambda = 200$ and 600 nm using an Agilent Cary 5000 UV/Vis/NIR spectrophotometer. Because of the high absorptivity and concentrations of the mixtures, samples were prepared in a 0.01 mm short-path-length cuvette (20/C-Q-0.01, Starna) to minimize saturation of the photodetector relative to a cuvette with a standard 10 mm path length. Even with the cuvette that was used, CAN dilution was necessary in some cases in order to obtain σ_{ext} without photodetector saturation at shorter wavelengths. Spectra were obtained as a function of $[\text{CAN}]$ (0.047 to 0.526 M), $[\text{HNO}_3]$ (0 to 6.0 M), and $[\text{NaNO}_3]$ (0 to 4.0 M) to cover the approximate range of mixture compositions that were characterized in Section 2.2. The σ_{ext} -values of the mixtures were then calculated using the Beer-Lambert law and applied in the KinSim mechanism. Model outputs were obtained over a total experimental time of 14400 s at 1 s intervals.

3 Results and Discussion

The maximum NO_3 quantum yield (ϕ_{NO_3}) of UVA-irradiated CAN/ HNO_3 mixtures is obtained at 6.0 M HNO_3 (Martin and Stevens, 1978); thus, this mixture composition served as the basis from which additional characterization studies were conducted. We found that 0.5 M CAN was the approximate solubility limit in 6.0 M HNO_3 at 25°C. Because 1.1 M CAN is the solubility limit in H_2O and CAN is almost nearly in HNO_3 (Martin and Glass, 1970), 0.7 M CAN is the estimated solubility limit in 6.0 M HNO_3 in the absence of changes in ceric nitrate composition in solution. Thus, the reduction in CAN solubility (0.7 M \rightarrow 0.5 M) observed in our studies was presumably associated with significant conversion of CAN to dimeric ceric nitrates in 6.0 M HNO_3 (Blaustein and Gryder, 1957; Demars et al., 2015).

3.1 NO_3 characterization studies

Figure 2a shows time series of thiophene ($\text{C}_4\text{H}_4\text{S}$), 2,3-dihydrobenzofuran ($\text{C}_8\text{H}_8\text{O}$), cis-3-hexenyl acetate ($\text{C}_8\text{H}_{14}\text{O}_2$), isoprene (C_5H_8), dimethyl sulfide ($\text{C}_2\text{H}_6\text{S}$), 2,5-dimethylthiophene ($\text{C}_6\text{H}_8\text{S}$), α -pinene ($\text{C}_{10}\text{H}_{16}$), and guaiacol ($\text{C}_7\text{H}_8\text{O}_2$) concentrations following injection into the OFR and exposure to NO_3 generated in the photoreactor from irradiation of a mixture of 0.5 M CAN and 6.0 M HNO_3 at $I_{369} = 7 \times 10^{15}$ photons cm^{-2} s^{-1} . Here, concentrations of each VOC were first normalized

to the acetonitrile concentration to correct for changes in the syringe pump output over time and then normalized to the VOC
150 concentration prior to NO_3 exposure. Aside from $\text{C}_6\text{H}_8\text{S}$, whose relative decay was less pronounced than expected (Table
S1), and butanal ($\text{C}_4\text{H}_8\text{O}$, not shown), whose signal decreased by approximately 30% and did not recover for reasons that
are unclear, the oxidative loss of each tracer increased with increasing k_{NO_3} . Maximum tracer consumption was observed at
the beginning of the experiment due to maximum NO_3 production from $\text{Ce}^{(\text{IV})}$ irradiation. As the experiment progressed and
 $\text{Ce}^{(\text{IV})}$ was reduced to $\text{Ce}^{(\text{III})}$, the NO_3 concentration and corresponding VOC oxidative loss decreased. Compared to the
155 other VOCs, the initial increase in $\text{C}_{10}\text{H}_{16}$ and $\text{C}_7\text{H}_8\text{O}_2$ concentrations over the first 2 hours was delayed because of their
higher k_{NO_3} values that resulted in >95% consumption and lower sensitivity to changes in $[\text{NO}_3]$ in the initial stage of the
experiment. To confirm that VOC degradation shown in Fig. 2a was due to reaction with NO_3 , Figure S3 shows the relative
 NO_3 rate coefficients obtained from the decay of $\text{C}_4\text{H}_4\text{S}$, $\text{C}_8\text{H}_8\text{O}$, and $\text{C}_8\text{H}_{14}\text{O}_2$ measured with the Vocus PTR. We measured
relative rate coefficients of 3.59 between $\text{C}_8\text{H}_8\text{O}$ and $\text{C}_4\text{H}_4\text{S}$ and 6.92 between $\text{C}_8\text{H}_{14}\text{O}_2$ and $\text{C}_4\text{H}_4\text{S}$, which are in agree-
160 ment with relative rate coefficient values of 3.44 ± 1.20 and 7.68 ± 2.84 calculated from their absolute NO_3 rate coefficients
(Atkinson, 1991; D'Anna et al., 2001). Time series of ions corresponding to nitrothiophene ($\text{C}_4\text{H}_3\text{NO}_2\text{S}$), $\text{C}_5\text{H}_7\text{NO}_{4-6}$ and
 $\text{C}_{10}\text{H}_{15}\text{NO}_{5,6}$ organic nitrates, and nitroguaiacol ($\text{C}_7\text{H}_7\text{NO}_4$), which are known NO_3 oxidation products of $\text{C}_4\text{H}_4\text{S}$, C_5H_8 ,
 $\text{C}_{10}\text{H}_{16}$, and $\text{C}_7\text{H}_8\text{O}_2$ (Atkinson et al., 1990; Jenkin et al., 2003; Saunders et al., 2003; Cabañas et al., 2005), along with
 $\text{C}_8\text{H}_{5,7}\text{NO}_{4-6}$ and $\text{C}_8\text{H}_{13}\text{NO}_{5-6}$ ions that may be associated with NO_3 oxidation products of $\text{C}_8\text{H}_8\text{O}$ and $\text{C}_8\text{H}_{14}\text{O}_2$, respec-
165 tively, were anticorrelated with those of their respective VOC precursors (Figure S4). Tracer decay experiments similar to the
one shown in Figure S3 were used to obtain results that are discussed in more detail in Sections 3.2, 3.3, and 3.4.

3.2 Effect of irradiation wavelength

Figure 3a shows normalized $[\text{NO}_3]$ values obtained following irradiation of mixtures containing CAN and 6.0 M HNO_3
or 4.8 M NaNO_3 as a function of irradiation wavelength. In CAN/ HNO_3 mixtures, $[\text{NO}_3]$ was a factor of 2.4-3.5 higher
170 following irradiation at $\lambda = 369$ compared to the other wavelengths. On the other hand, $[\text{NO}_3]$ decreased with increasing
irradiation wavelength following irradiation of CAN/ NaNO_3 mixtures; at $\lambda = 254$ nm, $[\text{NO}_3]$ was a factor of 3.2-42 times
higher than at the other irradiation wavelengths that were used. These differences in $[\text{NO}_3]$ were larger than the differences in
calibrated ~~I -values~~ photon flux values at the maximum ~~output~~ output of each lamp type ($\pm 40\%$; Sect. 2.1). Different $\text{Ce}^{(\text{IV})}$
in CAN/ HNO_3 and CAN/ NaNO_3 mixtures may have influenced these trends, as suggested by their UV/Vis spectra (Fig. 3b).
175 The σ_{ext} curves of CAN/ HNO_3 mixtures were generally larger, broader, and red-shifted relative to those of CAN/ NaNO_3
mixtures, with the extent of red-shifting increasing with increasing $[\text{HNO}_3]$, possibly due to higher yields of $\text{Ce}(\text{NO}_3)_6^{2-}$
and/or ceric nitrate dimers (Blaustein and Gryder, 1957; Henshall, 1963; Demars et al., 2015). For $\lambda > 250$ nm, CAN/ HNO_3
mixtures had $\sigma_{\text{ext,max}}$ values between $\lambda = 306 - 311$ nm, whereas CAN/ NaNO_3 solutions had $\sigma_{\text{ext,max}}$ values at $\lambda = 296$ nm.
However, if $[\text{NO}_3]$ was simply proportional to σ_{ext} , irradiation of CAN/ HNO_3 mixtures at $\lambda = 313$ nm should have produced
180 the highest $[\text{NO}_3]$; this was not the case. Instead, model calculations suggest that higher $[\text{NO}_2]$ obtained from significantly
faster photolysis of HNO_3 at $\lambda = 254$ and 313 nm relative to $\lambda > 350$ nm suppressed NO_3 downstream of the photoreactor
when shorter irradiation wavelengths were used (Sander et al. (2011), Table S2). At a photon flux of 10^{16} photons $\text{cm}^{-2} \text{s}^{-1}$,

model-calculated $[\text{NO}_3]$ values were within $\pm 13\%$ of each other for irradiation wavelengths ranging from $\lambda = 254$ to 369 nm. However, higher $[\text{NO}_2]$ values obtained following $\text{Ce}^{(\text{IV})}$ irradiation at $\lambda = 254$ and 313 nm suppressed NO_3 by $>96\%$ relative to the $\lambda = 369$ nm case during 120 s of simulated $\text{NO}_2 + \text{NO}_3$ reactions in the OFR. Thus, although the measured NO_3 suppression at these other irradiation wavelengths was less substantial than the model output, the measurement and model trends, along with achievement of maximum $[\text{NO}_3]$ following $\lambda = 254$ nm irradiation of CAN/ NaNO_3 mixtures that had lower $[\text{HNO}_3]$, qualitatively support this explanation for the wavelength-dependent NO_3 yields observed in CAN/ HNO_3 mixtures.

3.3 Effect of mixture composition

To characterize the influence of individual reagents on NO_3 formation, tracer decay experiments similar to the measurements shown in Figure 2 were repeated as a function of $[\text{CAN}]$, $[\text{HNO}_3]$, and $[\text{NaNO}_3]$. Figure 4a shows $[\text{NO}_3]$ obtained from irradiated 6.0 M HNO_3 solutions containing 0.001 to 0.5 M CAN ($I_{369} = 7 \times 10^{15}$ photons $\text{cm}^{-2} \text{s}^{-1}$), and irradiated 1.0 M NaNO_3 solutions containing 0.5 to 1.0 M CAN ($I_{254} = 1 \times 10^{16}$ photons $\text{cm}^{-2} \text{s}^{-1}$). Results were normalized to $[\text{NO}_3]$ achieved with solutions containing 0.5 M CAN and 6.0 M HNO_3 . Control experiments conducted with irradiated 6.0 M HNO_3 or 1.0 M NaNO_3 solutions at $I_{254} = 1 \times 10^{16}$ photons $\text{cm}^{-2} \text{s}^{-1}$ in the absence of CAN suggest that a fraction of the NO_3 obtained in CAN mixtures was generated via the reactions $\text{HNO}_3 + h\nu \rightarrow \text{OH} + \text{NO}_2$ and $\text{HNO}_3 + \text{OH} \rightarrow \text{NO}_3 + \text{H}_2\text{O}$. The remaining NO_3 was clearly obtained from CAN irradiation because $[\text{NO}_3]$ increased with increasing $[\text{CAN}]$, as expected from Reaction R1. Overall, $[\text{NO}_3]$ increased by approximately a factor of 3 as $[\text{CAN}]$ was increased from 0.001 to 0.5 M in 6.0 M HNO_3 .

Figure 4b shows $[\text{NO}_3]$ obtained in irradiated solutions containing 0.5 M CAN as a function of $[\text{HNO}_3]$ ranging from 1.0 to 6.0 M or $[\text{NaNO}_3]$ ranging from 1.0 to 4.8 M at the same I_{369} and I_{254} values used to obtain results shown in Fig. 4a. Irradiated CAN solutions containing 3.0 M and 6.0 M HNO_3 generated the same $[\text{NO}_3]$ concentrations within measurement uncertainties, presumably because the NO_3 quantum yield (ϕ_{NO_3}) ranged from 0.92-1.00 over this range of acidity (Martin and Stevens, 1978; Wine et al., 1988). $[\text{NO}_3]$ decreased by a factor of 2 as $[\text{HNO}_3]$ was decreased from 3.0 M to 1.0 M, consistent with a reduction in ϕ_{NO_3} from 0.92 to 0.46 (Martin and Stevens, 1978). On the other hand, in irradiated CAN/ NaNO_3 mixtures with uncharacterized ϕ_{NO_3} , $[\text{NO}_3]$ was constant within measurement uncertainties between 1.0 and 4.8 M NaNO_3 .

Other mixture components that were tested or considered included substitution of CH_3CN in place of H_2O and HNO_3 , ammonium nitrate (NH_4NO_3) instead of NaNO_3 , ceric potassium nitrate ($\text{K}_2\text{Ce}(\text{NO}_3)_6$) instead of CAN, and addition of sodium persulfate ($\text{Na}_2\text{S}_2\text{O}_8$) to generate additional NO_3 via $\text{S}_2\text{O}_8^{2-} + h\nu \rightarrow 2\text{SO}_4^-$ followed by $\text{SO}_4^- + \text{NO}_3^- \rightarrow \text{NO}_3 + \text{SO}_4^{2-}$ (Gaillard de Sémainville et al., 2007). CAN/ CH_3CN mixtures are commonly used in organic synthesis applications, perhaps even more so than CAN/ HNO_3 (Bacocchi et al., 1988; Choidini et al., 1993; Alexander, 2004). In limited testing, CAN/ CH_3CN appeared to generate significantly less NO_3 than CAN/ HNO_3 or CAN/ NaNO_3 , possibly due to lower ϕ_{NO_3} of irradiated $\text{Ce}^{(\text{IV})}$ - CH_3CN complexes (Glebov et al., 2021) and/or suppression of NO_3 due to its reaction with CH_3CN in solution. $\text{K}_2\text{Ce}(\text{NO}_3)_6$ is less widely available and less water-soluble than CAN and so was not considered further. Irradiation of CAN/ NH_4NO_3 and CAN/ NaNO_3 mixtures generated similar $[\text{NO}_3]$, but we prefer NaNO_3 due to its lower volatility.

Finally, ternary mixtures containing 0.5 M CAN + 2.0 M NaNO₃ + 0.5 M Na₂S₂O₈ irradiated at $\lambda = 254$ nm generated negligible additional NO₃ compared to binary CAN/NaNO₃ mixtures.

3.4 Effect of photon flux

Figure 5 shows normalized [NO₃] values obtained from ~~UVA-light-irradiated~~ irradiated mixtures of 0.5 M CAN & 6.0 M HNO₃ ~~and UVC-light-irradiated mixtures of~~ ($\lambda = 369$ nm) and 0.5 M CAN & 1.0 M NaNO₃ ($\lambda = 254$ nm) as a function of photon flux ranging from 6.9×10^{14} to 7.5×10^{15} photons cm⁻² s⁻¹. Results for both CAN/HNO₃ and CAN/NaNO₃ mixtures were normalized to [NO₃] achieved with 0.5 M CAN, 6.0 M HNO₃ and $I_{369} = 6.8 \times 10^{15}$ photons cm⁻² s⁻¹. Symbols are colored by the NO₃ lifetime (τ_{NO_3}), defined here as the time it took for [NO₃] to experience one e-fold decay relative to the maximum [NO₃] that was measured. Figure 5 shows that [NO₃] increased with increasing photon flux, consistent with the fact that it is a primary photolysis product, along with a concurrent decrease in τ_{NO_3} due to faster reduction of Ce(IV) to Ce(III). For the CAN/HNO₃ system, [NO₃] increased by a factor of 1.5 as I_{369} was increased from 6.9×10^{14} to 6.8×10^{15} photons cm⁻² s⁻¹, in agreement with the model-calculated increase in [NO₃] within measurement uncertainty. τ_{NO_3} decreased from 9 to 5 hr. For the CAN/NaNO₃ system, [NO₃] increased by a factor of 1.9 as I_{254} was increased from 1.0×10^{15} to 7.5×10^{15} photons cm⁻² s⁻¹, and τ_{NO_3} decreased from 10 to 3 hr.

To examine concentrations of NO₃ and a subset of additional gas-phase photolysis products obtained over a wider range of conditions, Figure 6 plots model-calculated [NO₃], NO₂:NO₃, HO₂:NO₃, and N₂O₅:NO₃ values as a function of photon flux ranging from 1×10^{14} to 1×10^{17} photons cm⁻² s⁻¹ following $\lambda = 254, 313, 369$ and 421 nm irradiation of a mixture of 0.5 M CAN and 6.0 M HNO₃. Figure 6a also plots the measured [NO₃] obtained from irradiation of a mixture of 0.5 M CAN and 6.0 M HNO₃ at $I_{369} = 7 \times 10^{15}$ photons cm⁻² s⁻¹ (Fig. 2) after correcting for dilution between the photoreactor and the OFR (Sect. 2.2) and application of a NO₃ wall loss rate coefficient of 0.2 s⁻¹ within the photoreactor (Dubé et al., 2006). At this photon flux value, the model-calculated [NO₃] = 1.4 ppmv agrees with [NO₃] = 1.7 ± 0.6 ppmv obtained from measurements. When considering only the primary photochemical process (Reactions R1-R5), maximum [NO₃] values within $\pm 10\%$ of each other were achieved at photon fluxes ranging from 5×10^{15} ($\lambda = 313$ nm) to 4×10^{16} photons cm⁻² s⁻¹ ($\lambda = 421$ nm). [NO₃] values decreased at higher ~~I -values~~ photon flux values due to conversion of NO₃ to NO₂ via photolysis. As shown in Fig. 6b, significant additional NO₂ production was obtained via HNO₃ photolysis at shorter irradiation wavelengths above $I \approx 10^{15}$ photons cm⁻² s⁻¹, resulting in NO₂:NO₃ > 10 ($\lambda = 254$ nm) and 1 ($\lambda = 313$ nm). Given additional reaction time downstream of the photoreactor, high NO₂ may suppress NO₃ (Sect. 3.2) and increase N₂O₅:NO₃ beyond the range of values shown in Fig. 6c. We also calculated OH:NO₃ and HO₂:NO₃ following irradiation of CAN/HNO₃ mixtures over the range of conditions shown in Figure 6. Aqueous OH:NO₃ ≈ 0.1 and did not change significantly as a function of photon flux or irradiation wavelength, and aqueous HO₂:NO₃ values ranged from 0.05 ($\lambda = 254$ nm) to 0.25 ($\lambda \geq 369$ nm). While OH influenced aqueous-phase chemistry inside the photoreactor via formation of reactive oxygen species (Sect. 3.5), OH probably did not influence downstream gas-phase chemistry due to significant wall losses inside the photoreactor: assuming a lower-limit OH wall loss rate coefficient of 5 s⁻¹ (Schwab et al., 1989), the estimated OH penetration efficiency through the reactor was

less than 10^{-6} . Similarly, in studies involving the generation of via VOC + reactions, is unlikely to significantly influence fate because + reactions are several times slower than those of + reactions (Orlando and Tyndall, 2012).

3.5 Characterization of reactive nitrogen and reactive oxygen photolysis products

Figure S5-7 shows time series of NO_2 , NO_3 , HNO_3 , and NO obtained with the CIMS reactive nitrogen and reactive oxygen species detected following irradiation of a the same mixture of 0.5 M CAN and 1.0 M NaNO_3 ($I_{254} \approx 10^{16}$ photons cm^{-2} s^{-1}). Signals of NO_2 and NO_3 decreased following irradiation of the CAN/mixture, whereas HNO_3 and NO signals increased. One potential source of NO_2 + reactions in the CIMS ion-molecule reactor (IMR); if this reaction was the sole source of here, we estimate an upper limit mixing ratio of approximately 15 ppbv present in the IMR (Dörich et al., 2021). NO_2 is generated following the reaction of and/or with (Abida and Osthoff, 2011), and is generated from the reaction of and/or with multiple nitrogen oxides, including NO , NO_2 , and NO_3 (Huey et al., 1995; Veres et al., 2015; Dörich et al., 2021), all of which are generated following irradiation as discussed later in this section. Figure 7 shows time-series of reactive nitrogen and reactive oxygen species detected following irradiation of the same mixture of 0.5 M CAN and 1.0 M NaNO_3 , shown here because the signal-to-noise in CIMS measurements of irradiated CAN/ NaNO_3 mixtures was generally better than in measurements of irradiated CAN/ HNO_3 mixtures due to reagent ion depletion by HNO_3 . A time series of $[\text{NO}_3]$ obtained separately from VOC tracer decay measurements under similar irradiation conditions is also shown. The NO_2 mixing ratio reached a maximum value and NO_3 mixing ratios reached maximum values of 26 and 58 ppbv shortly after the lights were turned on (Fig. 7a), suggesting an initial $\text{NO}_2:\text{NO}_3 \approx 0.37\text{--}0.45$ (Fig. 4) that was similar to modeled ≈ 0.33 obtained from irradiated CAN/(Fig. 6). Multiple reactions may generate NO_2 , including Reaction R3, HNO_3 and/or NO_3 photolysis, and other reactions listed in Table S2. While NO_2 and/or HNO_2 photolysis generated NO , its concentration was negligible in these experiments.

Figure 7b shows time series of IN_2O_5^- and IN_2O_6^- signals measured with the CIMS. Figure S5 additionally shows a time series of NO_2 and NO_3 , and Figures S6, S7, and S8 shows high-resolution CIMS spectra at $m/Q = 235, 251, \text{ and } 267$. IN_2O_5^- was formed from $\text{NO}_2 + \text{NO}_3 \rightarrow \text{N}_2\text{O}_5$ reactions in the photoreactor and $\text{N}_2\text{O}_5 + \text{I}^- \rightarrow \text{IN}_2\text{O}_5^-$ reactions in the CIMS IMR. As expected, IN_2O_5^- followed a similar profile as NO_2 and NO_3 . Given $\approx 10^{-3}$ coupled with similar and temporal profiles (Fig. S5), we hypothesize that + reactions in the IMR were the primary source of IN_2O_5^- . IN_2O_6^- was either generated from $\text{NO}_3 + \text{NO}_3 \rightarrow \text{N}_2\text{O}_6$ reactions in the photoreactor (Glass and Martin, 1970) followed by $\text{N}_2\text{O}_6 + \text{I}^- \rightarrow \text{IN}_2\text{O}_6^-$ reactions in the IMR, or from the following series of reactions in the IMR: $\text{HNO}_3 + \text{IO}^- \rightarrow \text{NO}_3^- + \text{HOI}$, $\text{HOI} + \text{NO}_3^- \rightarrow \text{INO}_3 + \text{OH}^-$, and $\text{INO}_3 + \text{NO}_3^- \rightarrow \text{IN}_2\text{O}_6^-$ (Ganske et al., 2019). If INO_3 is related to NO_2 , its signal increased faster than because INO_3 is a primary photolysis product, then decreased faster than because the production rate decreased quadratically as a function of decreasing NO_2 , whereas the production rate remained constant following processes that converted NO_2 to NO_3 . Additionally, because the aqueous phase + reaction rate is approximately 2000 times slower than that of + (Martin and Stevens, 1978; Katsumura et al., 1991), even a small amount of INO_3 would favor the formation of IN_2O_6^- compared to IN_2O_5^- . To further explore the plausibility of N_2O_6 formation in this system, we conducted a theoretical investigation of the gas-phase $\text{NO}_3 + \text{NO}_3 \rightarrow \text{N}_2\text{O}_6$ reaction at $T = 298$ K and $p = 1$ atm. Quantum-chemical calculations were performed using the Q-Chem 5.2 software package (Epifanovsky et al., 2021), and molecular geometries were obtained using the B3LYP density functional (Becke, 1993) and the 6-31G* basis set (Hariharan and Pople, 1973). All

stationary points were refined by single point calculations applying the B3LYP density functional and the cc-pVTZ basis set (Dunning, 1989) as well as CCSD(T) (Jeziorski and Monkhorst, 1981) and the cc-pVTZ basis set. For $+ \rightarrow +$, the calculated enthalpy of reaction (ΔH_{rxn}) was $-35.8 \text{ kcal mol}^{-1}$ using the CCSD(T) method, and $-21.9 \text{ kcal mol}^{-1}$ using the B3LYP method. By comparison, we calculated ΔH_{rxn} values of -26.5 (CCSD(T)) and -18.1 (B3LYP) kcal mol^{-1} for the $+ \rightarrow +$ reaction; the corresponding energy change (ΔE_{rxn}) values agreed within 5% of previously obtained experimental and computational ΔE_{rxn} values for this reaction (Jitariu and Hirst, 2000; Glendening and Halpern, 2007). Thus, regardless of the quantum-chemical method that was used, $+ \rightarrow +$ appears to be an exothermic reaction and found that this reaction is exothermic, even more so than $\text{NO}_3 + \text{NO}_3 \rightarrow \text{N}_2\text{O}_5$. While the reverse reaction $\rightarrow 2$ is possible (although endothermic, as is $\rightarrow +$) our analysis suggests that the thermodynamically favored reaction pathway is $\rightarrow +$, which had ΔH_{rxn} values ranging from -7.02 (CCSD(T)) to -6.15 (B3LYP) kcal mol^{-1} . By contrast, the reaction $\rightarrow 2$ had $\Delta H_{\text{rxn}} = 5.28$ (CCSD(T)) $- 5.58$ (B3LYP) kcal mol^{-1} ; however, because $\rightarrow 2$ is fast (Poskrebyshev et al., 2001; Atkinson et al., 2004), the overall reaction $\rightarrow 2 +$ is the favored removal pathway in the gas phase, and in solution may occur in addition to or instead of Reaction R4. Additional details regarding this analysis are provided in Sect. S1.

Figure 7c shows time series of IHNO_2^- , $\text{HNO}_2\text{NO}_3^-$, IHNO_4^- , and $\text{HNO}_4\text{NO}_3^-$. These ions are associated with nitrous acid (HNO_2) and peroxyxynitric acid (HNO_4) respectively (Veres et al., 2015). Because rapid formation of $\text{HNO}_{2-4}\text{NO}_3^-$ ions was observed following $\text{Ce}^{(\text{IV})}$ irradiation, and because IO_x^- signals were relatively low (Sect. S2.1), we hypothesize that $\text{I}^- + \text{NO}_3$ charge transfer and/or $\text{I}^- + \text{HNO}_3$ reactions were the main source of NO_3^- (Lee et al., 2014) (Lee et al., 2014; Dörich et al., 2021), and that subsequent competitive $\text{NO}_3^- + \text{HNO}_{2-4}$ and $\text{I}^- + \text{HNO}_{2-4}$ reactions in the IMR generated both IHNO_{2-4}^- and $\text{HNO}_{2-4}\text{NO}_3^-$. HNO_4 was generated following the reactions $\text{HNO}_3 + \text{h}\nu \rightarrow \text{OH} + \text{NO}_2$, $\text{OH} + \text{NO}_3 \rightarrow \text{HO}_2 + \text{NO}_2$, and $\text{HO}_2 + \text{NO}_2 \rightarrow \text{HNO}_4$. This hypothesis is supported by the similarity between NO_2 and IHNO_4^- time series coupled with the relatively constant concentrations of HO_2 generated via $\text{OH} + \text{OH} \rightarrow \text{H}_2\text{O}_2$ and $\text{OH} + \text{H}_2\text{O}_2 \rightarrow \text{HO}_2 + \text{H}_2\text{O}$ reactions. H_2O_2 , detected as IH_2O_2^- , also behaved similarly as IHO_2^- (Figure 7d). HNO_2 had a different temporal profile than the other nitrogen oxides: IHNO_2^- increased throughout the experiment, and $\text{HNO}_2\text{NO}_3^-$ increased and then decreased. We hypothesize that $\text{NO}_2 + \text{NO}_2 \rightarrow \text{N}_2\text{O}_4$ and $\text{N}_2\text{O}_4 + \text{H}_2\text{O} \rightarrow \text{HNO}_2 + \text{HNO}_3$ reactions were the main source of HNO_2 (Sect. S2.2). was not detected with the CIMS following irradiation of aqueous, presumably because its hydrolysis rate was too fast (Park and Lee, 1988). In an attempt to decrease the hydrolysis rate, separate experiments were conducted in which the effluent of 40 g of irradiated solid CAN was sampled with the CIMS. At the sample sizes that were used, the solid CAN contained enough solvated and/or that its irradiation provided sufficient production of nitrogen oxides for CIMS detection. As shown in Figures S9, S10 and S11, CIMS, , , and signals were significantly higher following irradiation at $\lambda = 254 \text{ nm}$ than at the other wavelengths, and Fig. S12 confirms that was the dominant ion signal at $m/Q = 219$. Taken together, these observations support our hypothesis that was generated following fast hydrolysis in aqueous solution.

To compare measurements of reactive nitrogen and reactive oxygen species obtained from irradiated CAN/and CAN/mixtures, Figure S13 shows time series of the same ions plotted in Figure 7 following irradiation of a solution containing 0.5 M CAN and 3.0 M HNO_3 ($I_{369} \approx 7 \times 10^{15} \text{ photons cm}^{-2} \text{ s}^{-1}$). Here, 3.0 M HNO_3 was used because 6.0 M HNO_3 depleted the CIMS reagent ion too much ($\text{IHNO}_3^- : \text{I}^- \approx 15$) to achieve signal-to-noise that was sufficient for comparison to CAN/ NaNO_3 mix-

tures ($\text{IHNO}_3^-:\text{I}^- \approx 3$). The same gas-phase nitrogen oxides and reactive oxygen species were observed in this reaction system as with the irradiated CAN/ NaNO_3 mixture. The relative yields of each compound plotted in Figures 7 and S13 were within a factor of 3 of each other, although signals of nitrogen oxides and reactive oxygen species obtained from irradiated CAN/ HNO_3 mixtures decreased at a slower rate than the same compounds obtained from irradiated CAN/ NaNO_3 mixtures. These trends may be due to different $\text{Ce}^{(\text{IV})}$ composition (Fig. 3 and Sect. 3.2) and/or enhanced rate of $\text{Ce}^{(\text{III})} + \text{NO}_3 \rightarrow \text{Ce}^{(\text{IV})}$ reactions in HNO_3 relative to NaNO_3 (Reaction R2).

3.6 OVOC/SOA generation from β -pinene + NO_3

To demonstrate proof of principle for NO_3 -initiated oxidative aging studies, we generated NO_3 via irradiation of a mixture of 0.5 M CAN and 3.0 M HNO_3 ($I_{369} = 7 \times 10^{15}$ photons $\text{cm}^{-2} \text{s}^{-1}$), reacted it with β -pinene in a dark OFR, and obtained FIGAERO-CIMS spectra of gas- and condensed-phase β -pinene + NO_3 oxidation products (Sect. 2.2). Figure 8a shows a spectrum of gas-phase β -pinene/ NO_3 oxidation products detected between $m/Q = 320$ and 420, where the majority of the signal was observed; signals shown are unmodified $(\text{M}+\text{I})^-$ formulas. The largest ion detected was at $m/Q = 356$ ($\text{IC}_{10}\text{H}_{15}\text{NO}_5^-$), which represents a major first-generation dicarbonyl nitrate oxidation product with a relative abundance of 0.31 and a calculated saturation vapor pressure of 2×10^{-7} atm ($C^* = 1900 \mu\text{g m}^{-3}$; Claffin (2018)). Other ions corresponding to first-generation hydroxycarbonyl nitrate ($\text{IC}_{10}\text{H}_{17}\text{NO}_5^-$, $C^* = 95 \mu\text{g m}^{-3}$), tricarbonyl nitrate ($\text{IC}_{10}\text{H}_{15}\text{NO}_6^-$, $C^* = 35 \mu\text{g m}^{-3}$), hydroxydicarbonyl nitrate ($\text{IC}_{10}\text{H}_{17}\text{NO}_6^-$, $C^* = 4.7 \mu\text{g m}^{-3}$), and hydroxycarbonyl nitrate acid ($\text{IC}_{10}\text{H}_{17}\text{NO}_7^-$, $C^* = 0.29 \mu\text{g m}^{-3}$) products were detected in addition to $\text{IC}_9\text{H}_{13}\text{NO}_5^-$ and a suite of additional previously characterized C_8 and C_9 organic nitrates (Nah et al., 2016; Takeuchi and Ng, 2019; Shen et al., 2021). The $\text{IC}_{10}\text{H}_{16}\text{N}_2\text{O}_7^-$ dinitrate was obtained following reaction of the β -nitrooxyperoxy radical with NO or hydroxy dinitrate, which was also previously observed in FIGAERO-CIMS spectra of α -pinene/ NO_3 (Nah et al., 2016; Bates et al., 2022) SOA (Nah et al., 2016), was generated via an unknown reaction pathway. Because model-calculated $\text{NO}:\text{NO}_3$ was on the order of 10^{-5} under these conditions, its formation from the $\text{RO}_2 + \text{NO}_3$ reaction seems more likely (Orlando and Tyndall, 2012). Overall, the high molar yield and vapor pressure of $\text{C}_{10}\text{H}_{15}\text{NO}_5$ (Claffin, 2018) are consistent with it having the highest relative abundance in the gas phase (Fig. 8a), whereas the other C_{10} β -pinene oxidation products were semivolatile under our experimental conditions.

Figure 9a shows a spectrum of condensed-phase β -pinene/ NO_3 oxidation products obtained with the FIGAERO-CIMS; signals were averaged over the entire thermal desorption cycle and are plotted on logarithmic scale and represent unmodified $(\text{M}+\text{I})^-$ formulas. To aid interpretation of the major features of the spectrum, bands of ion signals corresponding to $\text{IC}_{10}\text{H}_{15}\text{NO}_x^-$, $\text{IC}_{20}\text{H}_{32}\text{N}_2\text{O}_x^-$, and $\text{IC}_{30}\text{H}_{47}\text{N}_3\text{O}_x^-$ oxidation products were highlighted and colored by the number of oxygen atoms in their chemical formulas. Here, the largest ion detected was at $m/Q = 372$ ($\text{IC}_{10}\text{H}_{15}\text{NO}_6^-$), which is the condensed-phase component of the same tricarbonyl nitrate detected in the gas-phase (Fig. 8a). $\text{IC}_{10}\text{H}_{15}\text{NO}_5^-$ and $\text{IC}_{10}\text{H}_{15}\text{NO}_{7-9}^-$ signals were also detected. The second largest ion signal was measured at $m/Q = 571$ ($\text{IC}_{20}\text{H}_{32}\text{N}_2\text{O}_9^-$), an acetal dimer obtained from the condensed-phase reaction of two $\text{C}_{10}\text{H}_{17}\text{NO}_5$ monomers followed by H_2O elimination (Claffin and Ziemann, 2018). Similar accretion reactions between other C_{10} organic nitrates yielded $\text{IC}_{20}\text{H}_{32}\text{N}_2\text{O}_8^-$ and $\text{IC}_{20}\text{H}_{32}\text{N}_2\text{O}_{10-13}^-$ signals. Likewise, reactions between C_{10} monomers and C_{20} dimers generated C_{30} trimers detected between $m/Q = 768 - 864$

($\text{IC}_{30}\text{H}_{47}\text{N}_3\text{O}_{12-18}^-$). The largest trimer-related ion, $\text{IC}_{30}\text{H}_{47}\text{N}_3\text{O}_{12}^-$, was generated from $\text{C}_{10}\text{H}_{17}\text{NO}_4 + \text{C}_{20}\text{H}_{32}\text{NO}_9 - \text{H}_2\text{O}$ or $\text{C}_{10}\text{H}_{17}\text{NO}_5 + \text{C}_{20}\text{H}_{32}\text{NO}_8 - \text{H}_2\text{O}$ reactions (Claffin and Ziemann, 2018). A fourth cluster of ion signals at $m/Q > 984$ was also observed. Unambiguous assignment of chemical formulae to these signals was challenging due to the limited range of
 355 the CIMS m/z calibration and lack of available information about $\text{C}_{>30}$ β -pinene/ NO_3 oxidation products. However, it seems plausible that these signals are associated with tetramers.

To compare our results with those obtained using a conventional NO_3 generation method (room temperature N_2O_5 thermal decomposition) in an environmental chamber study, Figures 8b and 9b show reference gas- and condensed-phase FIGAERO- I^- -CIMS spectra of OVOCs and SOA generated from NO_3 oxidation of β -pinene in the Georgia Tech environmental chamber
 360 (Takeuchi and Ng, 2019). The spectra obtained here and by Takeuchi and Ng (2019) exhibit an overall high degree of similarity, with linear correlation coefficients of 0.87 and 0.96 between the respective gas- and condensed-phase spectra. Clusters of $\text{IC}_{10}\text{H}_{15}\text{NO}_x^-$, $\text{IC}_{20}\text{H}_{32}\text{N}_2\text{O}_x^-$, and $\text{IC}_{30}\text{H}_{47}\text{N}_3\text{O}_x^-$ ion signals were present in both Figs. 9a and 9b. The main differences between the gas-phase spectra shown in Figs. 8a and 9a were the different abundances of $\text{IC}_{10}\text{H}_{17}\text{NO}_4^-$, a first-generation hydroxynitrate product (Claffin and Ziemann, 2018), and $\text{IC}_{10}\text{H}_{16}\text{N}_2\text{O}_7^-$. Because $\text{C}_{10}\text{H}_{17}\text{NO}_4$ is formed from $\text{RO}_2 + \text{RO}_2$ reactions (DeVault et al., 2022) and is sufficiently volatile ($\text{C}^* = 750 \mu\text{g m}^{-3}$) to partition into the gas phase (Claffin, 2018),
 365 differences in gas-phase $\text{C}_{10}\text{H}_{17}\text{NO}_4$ and $\text{C}_{10}\text{H}_{16}\text{N}_2\text{O}_7$ yields were likely related to differences in the relative ~~rates~~ importance of $\text{RO}_2 + \text{RO}_2$ ~~and~~ versus $\text{RO}_2 + \text{NO}_3$ reaction pathways in the study by Takeuchi and Ng (2019) compared to this work.

To further investigate the fate of RO_2 generated from $\text{VOC} + \text{NO}_3$ reactions as a function of CAN irradiation conditions, we calculated the fractional oxidative loss of generic alkyl and acyl RO_2 species due to reaction with HO_2 , NO_3 and NO_2
 370 ($F_{\text{RO}_2 + \text{HO}_2}$, $F_{\text{RO}_2 + \text{NO}_3}$, $F_{\text{RO}_2 + \text{NO}_2}$) using Equations 1-3:

$$F_{\text{RO}_2 + \text{HO}_2} = \frac{k_{\text{RO}_2 + \text{HO}_2} [\text{HO}_2]}{k_{\text{RO}_2 + \text{HO}_2} [\text{HO}_2] + k_{\text{RO}_2 + \text{NO}_3} [\text{NO}_3] + k_{\text{RO}_2 + \text{NO}_2} [\text{NO}_2]} \quad (1)$$

$$F_{\text{RO}_2 + \text{NO}_3} = \frac{k_{\text{RO}_2 + \text{NO}_3} [\text{NO}_3]}{k_{\text{RO}_2 + \text{HO}_2} [\text{HO}_2] + k_{\text{RO}_2 + \text{NO}_3} [\text{NO}_3] + k_{\text{RO}_2 + \text{NO}_2} [\text{NO}_2]} \quad (2)$$

$$F_{\text{RO}_2 + \text{NO}_2} = \frac{k_{\text{RO}_2 + \text{NO}_2} [\text{NO}_2]}{k_{\text{RO}_2 + \text{HO}_2} [\text{HO}_2] + k_{\text{RO}_2 + \text{NO}_3} [\text{NO}_3] + k_{\text{RO}_2 + \text{NO}_2} [\text{NO}_2]} \quad (3)$$

Here, $k_{\text{RO}_2 + \text{HO}_2}$, $k_{\text{RO}_2 + \text{NO}_3}$, and $k_{\text{RO}_2 + \text{NO}_2}$ are reaction rate coefficients for the corresponding $\text{RO}_2 + \text{HO}_2$, $\text{RO}_2 + \text{NO}_3$ and
 375 $\text{RO}_2 + \text{NO}_2$ forward reactions whose values are summarized in Table S3. Several simplifying assumptions were made. First, we assumed that $\text{RO}_2 + \text{NO}$ reactions were negligible. Second, we did not consider RO_2 isomerization/autooxidation and $\text{RO}_2 + \text{RO}_2$ reactions that are influenced by external factors. Third, we set $F_{\text{RO}_2 + \text{NO}_2} = 0$ for alkyl- RO_2 -generated RO_2NO_2 , which thermally decompose on timescales of seconds or less (Orlando and Tyndall, 2012). Fourth, we assumed that vapor wall losses of acyl- RO_2 -generated RO_2NO_2 were a minor RO_2 sink because the OFR residence time ($\tau_{\text{OFR}} \approx 120$ s, Sect. 2.2) was
 380 significantly shorter than their estimated wall loss timescale ($\tau_{\text{wall}} \approx 400$ s, Palm et al. (2016)). Figure A shows calculated

$F_{\text{RO}_2+\text{HO}_2}$, $F_{\text{RO}_2+\text{NO}_3}$, and $F_{\text{RO}_2+\text{NO}_2}$ values for alkyl-RO₂ and acyl-RO₂ as a function of photon flux over the range of NO₃ generation conditions presented in Fig. 6. For alkyl-RO₂, $F_{\text{RO}_2+\text{HO}_2}$ decreased and $F_{\text{RO}_2+\text{NO}_3}$ increased with increasing photon flux and decreasing irradiation wavelength. On the other hand, for acyl-RO₂, $F_{\text{RO}_2+\text{NO}_2}$ increased while $F_{\text{RO}_2+\text{HO}_2}$ and $F_{\text{RO}_2+\text{NO}_3}$ decreased over the same irradiation conditions. Overall, at the optimal NO₃ generation conditions (e.g. $\lambda = 369$ nm and $I_{369} \approx 10^{16}$ photons cm⁻² s⁻¹), our calculations suggest that $F_{\text{RO}_2+\text{HO}_2} \approx F_{\text{RO}_2+\text{NO}_3}$ (Fig. Ac) and that $F_{\text{RO}_2+\text{HO}_2} \approx F_{\text{RO}_2+\text{NO}_3} \approx F_{\text{RO}_2+\text{NO}_2}$ was significant for acyl-RO₂ (Fig. Ag).

4 Conclusions

Ce^(IV) irradiation complements NO₂ + O₃ reactions and N₂O₅ thermal dissociation as a customizable photolytic NO₃ source. Important method parameters were [CAN], [HNO₃] or [NaNO₃], UV intensity, and irradiation wavelength. By contrast, important parameters for NO₂+O₃ and N₂O₅-based methods are [O₃], [NO₂], temperature, and humidity. Because Ce^(IV) irradiation already generates NO₃ in aqueous solution, its performance is not hindered by humidity to the same extent (if at all) as N₂O₅-based methods, where hydrolysis of N₂O₅ to HNO₃ decreases the efficacy of the source. Additionally, the NO₃ + H₂O reaction rate in solution or on surfaces is slow relative to other NO₃ loss pathways. Another advantage of Ce^(IV) irradiation is that it does not involve the use of O₃ as a reagent, therefore eliminating the possibility of competing O₃ and NO₃ oxidation of compounds that are reactive towards both oxidants if NO₂+O₃ reactions and/or online N₂O₅ synthesis are used as the NO₃ source (Lambe et al., 2020). To identify optimal operating conditions for maximizing [NO₃], we characterized concentrations of NO₃ at [CAN] = 10⁻³ to 1 M, [HNO₃] = 1.0 to 6.0 M, [NaNO₃] = 1.0 to 4.8 M, photon flux = 6.9×10¹⁴ to 1.0×10¹⁶ photons cm⁻² s⁻¹, and irradiation wavelengths of $\lambda = 254, 313, 369,$ or 421 nm. With CAN/HNO₃ mixtures, maximum [NO₃] was achieved with [CAN] ≈ 0.5 M, [HNO₃] ≈ 3.0 to 6.0 M, and $I_{369} = 8 \times 10^{15}$ photons cm⁻² s⁻¹ (4.3 mW cm⁻²). With CAN/NaNO₃ mixtures, maximum [NO₃] was achieved with [CAN] ≈ 1.0 M, [NaNO₃] ≥ 1.0 M, and $I_{254} \approx 1 \times 10^{16}$ photons cm⁻² s⁻¹ (7.8 mW cm⁻²). Thus, for applications such as environmental chamber or OFR studies of NO₃-initiated oxidative aging processes, where significant NO₃ production over relatively short time periods is beneficial, irradiation of concentrated Ce^(IV) solutions at high photon flux is advantageous. Other applications that require sustained NO₃ production at lower concentrations and/or over longer time periods may benefit from using lower [Ce^(IV)] and photon flux. Overall, because Ce^(IV) irradiation generates NO₃ at room temperature using widely-available, low-cost reagents and light sources (including high power light-emitting diodes in addition to, or instead of, UV fluorescent lamps) it is easier to apply than other NO₃ generation techniques - especially in field studies - and it may therefore enable more widespread studies of NO₃ oxidation chemistry. Adapting a photoreactor to operate with continuous injection of fresh Ce^(IV) or alternative photolytic NO₃ precursors (e.g. Hering et al. (2015)) rather than in batch mode as was done here may further enhance its performance and will be investigated in future work.

Code and data availability. Data and KinSim mechanisms presented in this manuscript are available upon request. The KinSim kinetic solver is freely available at <http://tinyurl.com/kinsim-release>.

Author contributions. AL, BB, and PL conceived and planned the experiments. AL, BB, MA, and PL carried out the experiments. AL conceived, planned, and carried out the KinSim model simulations. NO and PZ conceived, planned, and carried out the quantum chemical
415 calculations. AL, BB, MT, NO, PZ, MC, DW, and PL contributed to the interpretation of the results. AL took the lead in writing the manuscript. All authors provided feedback on the manuscript.

Competing interests. At least one of the coauthors is a member of the editorial board of Atmospheric Chemistry and Physics.

Acknowledgements. This work was supported by the Atmospheric Chemistry Program of the National Science Foundation: grants AGS-2131368 and AGS-2148439 to Aerodyne Research, Inc.; AGS-2131458 to the Georgia Institute of Technology; AGS-2131084 to Yale
420 University; and AGS-2147893 to the University of Michigan. AL thanks Anita Avery, Jordan Krechmer, Timothy Onasch (Aerodyne) and Shreya Suri (Georgia Tech) for experimental assistance, Evgeni Glebov (Russian Academy of Sciences) for sharing published UV/Vis spectra of CAN/CH₃CN mixtures, and the following colleagues for helpful discussions: Harald Stark, Manjula Canagaratna (Aerodyne), Steve Brown (NOAA CSL), Hartmut Herrmann (TROPOS), William Brune (Pennsylvania State University), Tyson Berg (Colorado State University), Lasse Moormann (Max Planck Institute for Chemistry), Uta Wille (University of Melbourne), Burkhard Koenig (University
425 of Regensburg). [The authors thank the anonymous referee and Sergey Nizkorodov for their constructive comments during the manuscript review process.](#)

References

- Abida, O. and Osthoff, H. D.: On the pH dependence of photo-induced volatilization of nitrogen oxides from frozen solutions containing nitrate, *Geophysical Research Letters*, 38, <https://doi.org/https://doi.org/10.1029/2011GL048517>, 2011.
- 430 Alexander, A. J.: Reaction kinetics of nitrate radicals with terpenes in solution studied by cavity ring-down spectroscopy, *Chemical Physics Letters*, 393, 138–142, <https://doi.org/https://doi.org/10.1016/j.cplett.2004.06.027>, 2004.
- Atkinson, R.: Kinetics and Mechanisms of the Gas-Phase Reactions of the NO₃ Radical with Organic Compounds, *Journal of Physical and Chemical Reference Data*, 20, 459–507, <https://doi.org/http://dx.doi.org/10.1063/1.555887>, 1991.
- Atkinson, R., Arey, J., Zielinska, B., and Aschmann, S. M.: Kinetics and nitro-products of the gas-phase OH and NO₃ radical-
435 initiated reactions of naphthalene-d₈, fluoranthene-d₁₀, and pyrene, *International Journal of Chemical Kinetics*, 22, 999–1014, <https://doi.org/10.1002/kin.550220910>, 1990.
- Atkinson, R., Tuazon, E. C., Bridier, I., and Arey, J.: Reactions of NO₃-naphthalene adducts with O₂ and NO₂, *Int. J. Chem. Kinet.*, 26, 605–614, <https://doi.org/10.1002/kin.550260603>, 1994.
- Atkinson, R., Arey, J., Aschmann, S. M., Corchnoy, S. B., and Shu, Y.: Rate constants for the gas-phase reactions of cis-3-Hexen-1-ol, cis-
440 3-Hexenylacetate, trans-2-Hexenal, and Linalool with OH and NO₃ radicals and O₃ at 296 ± 2 K, and OH radical formation yields from the O₃ reactions, *International Journal of Chemical Kinetics*, 27, 941–955, <https://doi.org/https://doi.org/10.1002/kin.550271002>, 1995.
- Atkinson, R., Baulch, D. L., Cox, R. A., Crowley, J. N., Hampson, R. F., Hynes, R. G., Jenkin, M. E., Rossi, M. J., and Troe, J.: Evaluated kinetic and photochemical data for atmospheric chemistry: Volume I - gas phase reactions of O_x, HO_x, NO_x and SO_x species, *Atmospheric Chemistry and Physics*, 4, 1461–1738, <https://doi.org/10.5194/acp-4-1461-2004>, 2004.
- 445 Baciocchi, E., Del Giacco, T., Murgia, S., and Sebastiani, G.: The photochemical reaction of cerium(IV) ammonium nitrate with alkenes. Rate and mechanism for the addition of the nitrate radical to alkenes, *Tetrahedron*, 44, 6651–6660, [https://doi.org/https://doi.org/10.1016/S0040-4020\(01\)90103-6](https://doi.org/https://doi.org/10.1016/S0040-4020(01)90103-6), 1988.
- Badenes, M. P., Tucceri, M. E., and Cobos, C. J.: Role of the Recombination Channel in the Reaction between the HO and HO₂ Radicals, *J. Phys. Chem. A*, 121, 440–447, <https://doi.org/10.1021/acs.jpca.6b10427>, 2017.
- 450 Bates, K. H., Burke, G. J. P., Cope, J. D., and Nguyen, T. B.: Secondary organic aerosol and organic nitrogen yields from the nitrate radical (NO₃) oxidation of alpha-pinene from various RO₂ fates, *Atmospheric Chemistry and Physics*, 22, 1467–1482, <https://doi.org/10.5194/acp-22-1467-2022>, 2022.
- Becke, A. D.: Density-functional thermochemistry. III. The role of exact exchange, *The Journal of Chemical Physics*, 98, 5648–5652, <https://doi.org/10.1063/1.464913>, 1993.
- 455 Becker, E., Rahman, M. M., and Schindler, R. N.: Determination of the Rate Constants for the Gas Phase Reactions of NO₃ with H, OH and HO₂ Radicals at 298 K, *Berichte der Bunsengesellschaft für physikalische Chemie*, 96, 776–783, <https://doi.org/https://doi.org/10.1002/bbpc.19920960608>, 1992.
- Bedjanian, Y.: Temperature-dependent rate constant for the reaction of F atoms with HNO₃, *International Journal of Chemical Kinetics*, 51, 753–759, <https://doi.org/https://doi.org/10.1002/kin.21306>, 2019.
- 460 Bertram, T. H., Kimmel, J. R., Crisp, T. A., Ryder, O. S., Yatavelli, R. L. N., Thornton, J. A., Cubison, M. J., Gonin, M., and Worsnop, D. R.: A field-deployable, chemical ionization time-of-flight mass spectrometer, *Atmospheric Measurement Techniques*, 4, 1471–1479, 2011.

- Birks, J. W., Andersen, P. C., Williford, C. J., Turnipseed, A. A., Strunk, S. E., Ennis, C. A., and Mattson, E.: Folded tubular photometer for atmospheric measurements of NO₂ and NO, *Atmospheric Measurement Techniques*, 11, 2821–2835, <https://doi.org/10.5194/amt-11-2821-2018>, 2018.
- 465 Blaustein, B. D. and Gryder, J. W.: An Investigation of the Species Existing in Nitric Acid Solutions Containing Cerium(III) and Cerium(IV)1, *J. Am. Chem. Soc.*, 79, 540–547, <https://doi.org/10.1021/ja01560a012>, 1957.
- Brown, S. S. and Stutz, J.: Nighttime radical observations and chemistry, *Chem. Soc. Rev.*, 41, 6405–6447, <https://doi.org/10.1039/C2CS35181A>, 2012.
- Brown, S. S., Dibb, J. E., Stark, H., Aldener, M., Vozella, M., Whitlow, S., Williams, E. J., Lerner, B. M., Jakoubek, R., Middlebrook, A. M.,
470 DeGouw, J. A., Warneke, C., Goldan, P. D., Kuster, W. C., Angevine, W. M., Sueper, D. T., Quinn, P. K., Bates, T. S., Meagher, J. F., Fehsenfeld, F. C., and Ravishankara, A. R.: Nighttime removal of NO_x in the summer marine boundary layer, *Geophysical Research Letters*, 31, <https://doi.org/https://doi.org/10.1029/2004GL019412>, 2004.
- Burrows, J. P., Tyndall, G. S., and Moortgat, G. K.: Absorption spectrum of NO₃ and kinetics of the reactions of NO₃ with NO₂, Cl, and several stable atmospheric species at 298 K, *J. Phys. Chem.*, 89, 4848–4856, <https://doi.org/10.1021/j100268a038>, 1985.
- 475 Cabañas, B., Baeza, M. T., Martín, P., Salgado, S., Villanueva, F., Monedero, E., and Wirtz, K.: Products and Mechanism of the NO₃ Reaction with Thiophene, *Journal of Atmospheric Chemistry*, 51, 317–335, <https://doi.org/10.1007/s10874-005-3580-5>, 2005.
- Cabañas, B., Baeza, M., Martín, P., Salgado, S., Villanueva, F., Monedero, E., and Díaz De Mera, Y.: Reaction of the NO₃ radical with some thiophenes: Kinetic study and a correlation between rate constant and EHOMO, *International Journal of Chemical Kinetics*, 38, 570–576, <https://doi.org/https://doi.org/10.1002/kin.20187>, 2006.
- 480 Cantrell, C. A., Davidson, J. A., Shetter, R. E., Anderson, B. A., and Calvert, J. G.: Reactions of nitrate radical and nitrogen oxide (N₂O₅) with molecular species of possible atmospheric interest, *The Journal of Physical Chemistry*, 91, 6017–6021, <https://doi.org/10.1021/j100307a040>, 1987.
- Choidini, G., Rindone, B., Cariati, F., Polesello, S., Restelli, G., and Hjorth, J.: Comparison between the gas-phase and the solution reaction of the nitrate radical and methylarenes, *Environ. Sci. Technol.*, 27, 1659–1664, <https://doi.org/10.1021/es00045a024>, 1993.
- 485 Clafin, M. S.: Role of Multiphase Chemistry on the Formation of Aerosol from the Reactions of Monoterpenes with NO₃ Radicals and O₃, Ph.D. thesis, University of Colorado, 2018.
- Clafin, M. S. and Ziemann, P. J.: Identification and Quantitation of Aerosol Products of the Reaction of beta-Pinene with NO₃ Radicals and Implications for Gas- and Particle-Phase Reaction Mechanisms, *The Journal of Physical Chemistry A*, 122, 3640–3652, <https://doi.org/10.1021/acs.jpca.8b00692>, PMID: 29528647, 2018.
- 490 Daniels, M.: Radiation chemistry of the aqueous nitrate system. III. Pulse electron radiolysis of concentrated sodium nitrate solutions, *J. Phys. Chem.*, 73, 3710–3717, <https://doi.org/10.1021/j100845a027>, 1969.
- D’Anna, B., Andresen, Ø., Gefen, Z., and Nielsen, C. J.: Kinetic study of OH and NO₃ radical reactions with 14 aliphatic aldehydes, *Phys. Chem. Chem. Phys.*, 3, 3057–3063, <https://doi.org/10.1039/B103623H>, 2001.
- Demars, T. J., Bera, M. K., Seifert, S., Antonio, M. R., and Ellis, R. J.: Revisiting the Solution Structure of Ceric Ammonium Nitrate, *Angewandte Chemie International Edition*, 54, 7534–7538, <https://doi.org/https://doi.org/10.1002/anie.201502336>, 2015.
- 495 DeMore, W., Sander, S., Golden, D., Hampson, R., Kurylo, M., Howard, C., Ravishankara, A., Kolb, C., and Molina, M.: Chemical Kinetic and Photochemical Data for Use in Stratospheric Modeling: Evaluation No. 11 of the NASA Panel for Data Evaluation, JPL Publication 94-26, 1994.

DeMore, W. B., Sander, S. P., Golden, D. M., Hampson, R. F., Kurylo, M. J., Howard, C. J., Ravishankara, A. R., Kolb, C. E., and Molina,
500 M. J.: Chemical kinetics and photochemical data for use in stratospheric modeling. Evaluation number 12, JPL Publication 97-4, 1997.

DeVault, M. P., Ziola, A. C., and Ziemann, P. J.: Products and Mechanisms of Secondary Organic Aerosol Formation
from the NO₃ Radical-Initiated Oxidation of Cyclic and Acyclic Monoterpenes, ACS Earth Space Chem., 6, 2076–2092,
<https://doi.org/10.1021/acsearthspacechem.2c00130>, 2022.

Dörich, R., Eger, P., Lelieveld, J., and Crowley, J. N.: Iodide CIMS and *m/z* 62: the detection of HNO₃ as NO₃⁻ in the presence of PAN,
505 peroxyacetic acid and ozone, Atmospheric Measurement Techniques, 14, 5319–5332, <https://doi.org/10.5194/amt-14-5319-2021>, 2021.

Dubé, W. P., Brown, S. S., Osthoff, H. D., Nunley, M. R., Ciciora, S. J., Paris, M. W., McLaughlin, R. J., and Ravishankara, A. R.: Aircraft
instrument for simultaneous, in situ measurement of NO₃ and N₂O₅ via pulsed cavity ring-down spectroscopy, Review of Scientific
Instruments, 77, 34–101, <https://doi.org/10.1063/1.2176058>, 2006.

Dunning, Thom H., J.: Gaussian basis sets for use in correlated molecular calculations. I. The atoms boron through neon and hydrogen, The
510 Journal of Chemical Physics, 90, 1007–1023, <https://doi.org/10.1063/1.456153>, 1989.

Elliot, A. J. and Buxton, G. V.: Temperature dependence of the reactions OH + O and OH + HO₂ in water up to 200 °C, J. Chem. Soc.,
Faraday Trans., 88, 2465–2470, <https://doi.org/10.1039/FT9928802465>, 1992.

Elliot, A. J., McCracken, D. R., Buxton, G. V., and Wood, N. D.: Estimation of rate constants for near-diffusion-controlled reactions in water
at high temperatures, J. Chem. Soc., Faraday Trans., 86, 1539–1547, <https://doi.org/10.1039/FT9908601539>, 1990.

515 Epifanovsky, E., Gilbert, A. T. B., Feng, X., Lee, J., Mao, Y., Mardirossian, N., Pokhilko, P., White, A. F., Coons, M. P., Dempwolff, A. L.,
Gan, Z., Hait, D., Horn, P. R., Jacobson, L. D., Kaliman, I., Kussmann, J., Lange, A. W., Lao, K. U., Levine, D. S., Liu, J., McKenzie,
S. C., Morrison, A. F., Nanda, K. D., Plasser, F., Rehn, D. R., Vidal, M. L., You, Z.-Q., Zhu, Y., Alam, B., Albrecht, B. J., Aldossary, A.,
Alguire, E., Andersen, J. H., Athavale, V., Barton, D., Begam, K., Behn, A., Bellonzi, N., Bernard, Y. A., Berquist, E. J., Burton, H. G. A.,
Carreras, A., Carter-Fenk, K., Chakraborty, R., Chien, A. D., Closser, K. D., Cofer-Shabica, V., Dasgupta, S., de Wergifosse, M., Deng,
520 J., Diedenhofen, M., Do, H., Ehlert, S., Fang, P.-T., Fatehi, S., Feng, Q., Friedhoff, T., Gayvert, J., Ge, Q., Gidofalvi, G., Goldey, M.,
Gomes, J., González-Espinoza, C. E., Gulania, S., Gunina, A. O., Hanson-Heine, M. W. D., Harbach, P. H. P., Hauser, A., Herbst, M. F.,
Hernández Vera, M., Hodecker, M., Holden, Z. C., Houck, S., Huang, X., Hui, K., Huynh, B. C., Ivanov, M., Jász, A., Ji, H., Jiang, H.,
Kaduk, B., Kähler, S., Khistyayev, K., Kim, J., Kis, G., Klunzinger, P., Koczor-Benda, Z., Koh, J. H., Kosenkov, D., Koulias, L., Kowalczyk,
T., Krauter, C. M., Kue, K., Kunitsa, A., Kus, T., Ladjánszki, I., Landau, A., Lawler, K. V., Lefrancois, D., Lehtola, S., Li, R. R., Li, Y.-P.,
525 Liang, J., Liebenthal, M., Lin, H.-H., Lin, Y.-S., Liu, F., Liu, K.-Y., Loipersberger, M., Luenser, A., Manjanath, A., Manohar, P., Mansoor,
E., Manzer, S. F., Mao, S.-P., Marenich, A. V., Markovich, T., Mason, S., Maurer, S. A., McLaughlin, P. F., Menger, M. F. S. J., Mewes,
J.-M., Mewes, S. A., Morgante, P., Mullinax, J. W., Oosterbaan, K. J., Paran, G., Paul, A. C., Paul, S. K., Pavošević, F., Pei, Z., Prager,
S., Proynov, E. I., Rák, A., Ramos-Cordoba, E., Rana, B., Rask, A. E., Rettig, A., Richard, R. M., Rob, F., Rossomme, E., Scheele, T.,
Scheurer, M., Schneider, M., Sergueev, N., Sharada, S. M., Skomorowski, W., Small, D. W., Stein, C. J., Su, Y.-C., Sundstrom, E. J., Tao,
530 Z., Thirman, J., Tornai, G. J., Tsuchimochi, T., Tubman, N. M., Veccham, S. P., Vydrov, O., Wenzel, J., Witte, J., Yamada, A., Yao, K.,
Yeganeh, S., Yost, S. R., Zech, A., Zhang, I. Y., Zhang, X., Zhang, Y., Zuev, D., Aspuru-Guzik, A., Bell, A. T., Besley, N. A., Bravaya,
K. B., Brooks, B. R., Casanova, D., Chai, J.-D., Coriani, S., Cramer, C. J., Cserey, G., DePrince, A. E. r., DiStasio, R. A. J., Dreuw, A.,
Dunietz, B. D., Furlani, T. R., Goddard, W. A. r., Hammes-Schiffer, S., Head-Gordon, T., Hehre, W. J., Hsu, C.-P., Jagau, T.-C., Jung, Y.,
Klamt, A., Kong, J., Lambrecht, D. S., Liang, W., Mayhall, N. J., McCurdy, C. W., Neaton, J. B., Ochsenfeld, C., Parkhill, J. A., Peverati,
535 R., Rassolov, V. A., Shao, Y., Slipchenko, L. V., Stauch, T., Steele, R. P., Subotnik, J. E., Thom, A. J. W., Tkatchenko, A., Truhlar, D. G.,
Van Voorhis, T., Wesolowski, T. A., Whaley, K. B., Woodcock, H. L. r., Zimmerman, P. M., Faraji, S., Gill, P. M. W., Head-Gordon,

- M., Herbert, J. M., and Krylov, A. I.: Software for the frontiers of quantum chemistry: An overview of developments in the Q-Chem 5 package., *The Journal of chemical physics*, 155, 084 801, 2021.
- 540 Feng, P. Y., Brynjolfsson, A., Halliday, J. W., and Jarrett, R. D.: High-intensity radiolysis of aqueous ferrous sulfate-cupric sulfate-sulfuric acid solutions, *J. Phys. Chem.*, 74, 1221–1227, <https://doi.org/10.1021/j100701a011>, 1970.
- Gaillard de Sémainville, P., Hoffmann, D., George, C., and Herrmann, H.: Study of nitrate radical (NO₃) reactions with carbonyls and acids in aqueous solution as a function of temperature, *Phys. Chem. Chem. Phys.*, 9, 958–968, <https://doi.org/10.1039/B613956F>, 2007.
- Ganske, J. A., Wingen, L. M., Perraud, V., and Finlayson-Pitts, B. J.: Role of Gas-Phase Halogen Bonding in Ambient Chemical Ionization Mass Spectrometry Utilizing Iodine, *ACS Earth Space Chem.*, 3, 1315–1328, <https://doi.org/10.1021/acsearthspacechem.9b00030>, 2019.
- 545 Glass, R. W. and Martin, T. W.: Flash generation and decay kinetics of the nitrate radical in aqueous nitric acid solutions, *J. Am. Chem. Soc.*, 92, 5084–5093, <https://doi.org/10.1021/ja00720a014>, 1970.
- Glebov, E. M., Grivin, V. P., Plyusnin, V. F., Fedunov, R. G., Pozdnyakov, I. P., Yanshole, V. V., and Vasilchenko, D. B.: Photochemistry of cerium(IV) ammonium nitrate (CAN) in acetonitrile, *Journal of Photochemistry and Photobiology A: Chemistry*, 418, 113 440, <https://doi.org/https://doi.org/10.1016/j.jphotochem.2021.113440>, 2021.
- 550 Glendening, E. D. and Halpern, A. M.: Ab initio calculations of nitrogen oxide reactions: Formation of N₂O₂, N₂O₃, N₂O₄, N₂O₅, and N₄O₂ from NO, NO₂, NO₃, and N₂O, *The Journal of Chemical Physics*, 127, <https://doi.org/10.1063/1.2777145>, 164307, 2007.
- Goldstein, S. and Czapski, G.: The reaction of NO with O₂⁻ and HO₂⁻: a pulse radiolysis study, *Free radical biology & medicine*, 19, 505–10, 1995.
- Grätzel, M., Taniguchi, S., and Henglein, A.: Pulsradiolytische Untersuchung kurzlebiger Zwischenprodukte der NO-Reduktion in wäßriger Lösung, *Berichte der Bunsengesellschaft für physikalische Chemie*, 74, 1003–1010, <https://doi.org/https://doi.org/10.1002/bbpc.19700741012>, 1970.
- Halpern, J. and Rabani, J.: Reactivity of Hydrogen Atoms toward Some Cobalt(III) Complexes in Aqueous Solutions¹, *J. Am. Chem. Soc.*, 88, 699–704, <https://doi.org/10.1021/ja00956a015>, 1966.
- Hariharan, P. C. and Pople, J. A.: The influence of polarization functions on molecular orbital hydrogenation energies, *Theoretica chimica acta*, 28, 213–222, <https://doi.org/10.1007/BF00533485>, 1973.
- 560 Henshall, A.: The Photoreduction of Ceric Ammonium Nitrate in Glacial Acetic Acid Solution, Ph.D. thesis, Vanderbilt University, 1963.
- Hering, T., Slanina, T., Hancock, A., Wille, U., and König, B.: Visible light photooxidation of nitrate: the dawn of a nocturnal radical, *Chem. Commun.*, 51, 6568–6571, <https://doi.org/10.1039/C5CC01580D>, 2015.
- Herrmann, H., Exner, M., and Zellner, R.: Reactivity trends in reactions of the nitrate radical (NO₃) with inorganic and organic cloudwater constituents, *Geochimica et Cosmochimica Acta*, 58, 3239 – 3244, [https://doi.org/https://doi.org/10.1016/0016-7037\(94\)90051-5](https://doi.org/https://doi.org/10.1016/0016-7037(94)90051-5), 1994.
- Hinsvark, O. N. and Stone, K. G.: Oxidation of Oxalic Acid in Glacial Acetic Acid with Cerium(IV), *Anal. Chem.*, 28, 334–337, <https://doi.org/10.1021/ac60111a014>, 1956.
- Huey, L. G., Hanson, D. R., and Howard, C. J.: Reactions of SF₆⁻ and I⁻ with Atmospheric Trace Gases, *J. Phys. Chem.*, 99, 5001–5008, <https://doi.org/10.1021/j100014a021>, 1995.
- 570 Jenkin, M., Saunders, S., Wagner, V., and Pilling, M.: Protocol for the development of the Master Chemical Mechanism, MCM v3 (Part B): tropospheric degradation of aromatic volatile organic compounds, *Atmospheric Chemistry and Physics*, 3, 181–193, 2003.
- Jeziorski, B. and Monkhorst, H. J.: Coupled-cluster method for multideterminantal reference states, *Phys. Rev. A*, 24, 1668–1681, <https://doi.org/10.1103/PhysRevA.24.1668>, 1981.

- Jiang, P. Y., Katsumura, Y., Ishigure, K., and Yoshida, Y.: Reduction potential of the nitrate radical in aqueous solution, *Inorg. Chem.*, 31, 575 5135–5136, <https://doi.org/10.1021/ic00050a038>, 1992.
- Jitariu, L. C. and Hirst, D. M.: Theoretical investigation of the $\text{N}_2\text{O}_5 \rightleftharpoons \text{NO}_2 + \text{NO}_3$ equilibrium by density functional theory and ab initio calculations, *Phys. Chem. Chem. Phys.*, 2, 847–852, <https://doi.org/10.1039/A906864C>, 2000.
- Kahan, T. F., Washenfelder, R. A., Vaida, V., and Brown, S. S.: Cavity-Enhanced Measurements of Hydrogen Peroxide Absorption Cross Sections from 353 to 410 nm, *J. Phys. Chem. A*, 116, 5941–5947, <https://doi.org/10.1021/jp2104616>, 2012.
- 580 Katsumura, Y., Jiang, P. Y., Nagaishi, R., Oishi, T., Ishigure, K., and Yoshida, Y.: Pulse radiolysis study of aqueous nitric acid solutions: formation mechanism, yield, and reactivity of NO_3 radical, *J. Phys. Chem.*, 95, 4435–4439, <https://doi.org/10.1021/j100164a050>, 1991.
- Kebabian, P. L., Herndon, S. C., and Freedman, A.: Detection of Nitrogen Dioxide by Cavity Attenuated Phase Shift Spectroscopy, *Analytical Chemistry*, 77, 724–728, 2005.
- Krechmer, J., Lopez-Hilfiker, F., Koss, A., Hutterli, M., Stoermer, C., Deming, B., Kimmel, J., Warneke, C., Holzinger, R., Jayne, J., Worsnop, 585 D., Fuhrer, K., Gonin, M., and de Gouw, J.: Evaluation of a New Reagent-Ion Source and Focusing Ion-Molecule Reactor for Use in Proton-Transfer-Reaction Mass Spectrometry, *Analytical Chemistry*, 90, 12 011–12 018, <https://doi.org/10.1021/acs.analchem.8b02641>, PMID: 30220198, 2018.
- Lambe, A. T., Krechmer, J. E., Peng, Z., Casar, J. R., Carrasquillo, A. J., Raff, J. D., Jimenez, J. L., and Worsnop, D. R.: HO_x and NO_x production in oxidation flow reactors via photolysis of isopropyl nitrite, isopropyl nitrite- d_7 , and 1,3-propyl dinitrite at $\lambda = 254, 350,$ and 590 369 nm, *Atmospheric Measurement Techniques*, 12, 299–311, <https://doi.org/10.5194/amt-12-299-2019>, 2019.
- Lambe, A. T., Wood, E. C., Krechmer, J. E., Majluf, F., Williams, L. R., Croteau, P. L., Cirtog, M., Féron, A., Petit, J.-E., Albinet, A., Jimenez, J. L., and Peng, Z.: Nitrate radical generation via continuous generation of dinitrogen pentoxide in a laminar flow reactor coupled to an oxidation flow reactor, *Atmospheric Measurement Techniques*, 13, 2397–2411, <https://doi.org/10.5194/amt-13-2397-2020>, 2020.
- Lammel, G., Perner, D., and Warneck, P.: Decomposition of pernitric acid in aqueous solution, *J. Phys. Chem.*, 94, 6141–6144, 595 <https://doi.org/10.1021/j100378a091>, 1990.
- Lauraguais, A., El Zein, A., Coeur, C., Obeid, E., Cassez, A., Rayez, M.-T., and Rayez, J.-C.: Kinetic Study of the Gas-Phase Reactions of Nitrate Radicals with Methoxyphenol Compounds: Experimental and Theoretical Approaches, *J. Phys. Chem. A*, 120, 2691–2699, <https://doi.org/10.1021/acs.jpca.6b02729>, 2016.
- Lee, B. H., Lopez-Hilfiker, F. D., Mohr, C., Kurten, T., Worsnop, D. R., and Thornton, J. A.: An Iodide-Adduct High-Resolution Time-of- 600 Flight Chemical-Ionization Mass Spectrometer: Application to Atmospheric Inorganic and Organic Compounds, *Environmental Science and Technology*, 48, 6309–6317, 2014.
- Loegager, T. and Sehested, K.: Formation and decay of peroxyxynitrous acid: a pulse radiolysis study, *J. Phys. Chem.*, 97, 6664–6669, <https://doi.org/10.1021/j100127a016>, 1993.
- Lopez-Hilfiker, F. D., Mohr, C., Ehn, M., Rubach, F., Kleist, E., Wildt, J., Mentel, T. F., Lutz, A., Hallquist, M., Worsnop, D., and Thornton, 605 J. A.: A novel method for on-line analysis of gas and particle composition: description and evaluation of a Filter Inlet for Gases and AEROSols (FIGAERO), *Atmospheric Measurement Techniques Discussions*, 6, 9347–9395, 2013.
- Martin, T. W. and Glass, R. W.: Competitive electron transfer. Activity-defined formation constants of cerium(III) nitrate complexes based on reaction with the nitrate free radical, *J. Am. Chem. Soc.*, 92, 5075–5083, <https://doi.org/10.1021/ja00720a013>, 1970.
- Martin, T. W. and Stevens, M. V.: Studies Using a Combination of Flash Photolysis and Pulsed Magnetic Induction: Application to the 610 NO_3 Radical in Aqueous Acid Solution at 25°C, in: 12th Informal Conference on Photochemistry, National Bureau of Standards Special Publication 526, 1978.

- Martin, T. W., Henshall, A., and Gross, R. C.: Spectroscopic and Chemical Evidence for the NO₃ Free Radical in Solution at Room Temperature, *J. Am. Chem. Soc.*, 85, 113–114, <https://doi.org/10.1021/ja00884a027>, 1963.
- Martin, T. W., Rummel, R. E., and Gross, R. C.: Electron Exchange Kinetics of the NO₃ Free Radical in Solution, *J. Am. Chem. Soc.*, 86, 2595–2600, <https://doi.org/10.1021/ja01067a016>, 1964.
- 615 Meyer, R. J. and Jacoby, R.: Die Doppelnitrate des vierwertigen Ceriums und des Thoriums, *Zeitschrift für anorganische Chemie*, 27, 359–389, <https://doi.org/https://doi.org/10.1002/zaac.19010270131>, 1901.
- Mezyk, S. P. and Bartels, D. M.: Direct EPR measurement of Arrhenius parameters for the reactions of H· atoms with H₂O₂ and D· atoms with D₂O₂ in aqueous solution, *J. Chem. Soc., Faraday Trans.*, 91, 3127–3132, <https://doi.org/10.1039/FT9959103127>, 1995.
- 620 Morris, E. D. J. and Niki, H.: Reaction of dinitrogen pentoxide with water, *J. Phys. Chem.*, 77, 1929–1932, <https://doi.org/10.1021/j100635a001>, 1973.
- Nah, T., Sanchez, J., Boyd, C. M., and Ng, N. L.: Photochemical Aging of α -pinene and β -pinene Secondary Organic Aerosol formed from Nitrate Radical Oxidation, *Environmental Science & Technology*, 50, 222–231, <https://doi.org/10.1021/acs.est.5b04594>, PMID: 26618657, 2016.
- 625 Nair, V. and Deepthi, A.: Cerium(IV) Ammonium Nitrate A Versatile Single-Electron Oxidant, *Chem. Rev.*, 107, 1862–1891, <https://doi.org/10.1021/cr068408n>, 2007.
- Ng, N. L., Brown, S. S., Archibald, A. T., Atlas, E., Cohen, R. C., Crowley, J. N., Day, D. A., Donahue, N. M., Fry, J. L., Fuchs, H., Griffin, R. J., Guzman, M. I., Herrmann, H., Hodzic, A., Iinuma, Y., Jimenez, J. L., Kiendler-Scharr, A., Lee, B. H., Luecken, D. J., Mao, J., McLaren, R., Mutzel, A., Osthoff, H. D., Ouyang, B., Picquet-Varrault, B., Platt, U., Pye, H. O. T., Rudich, Y., Schwantes, R. H., Shiraiwa, M., Stutz, J., Thornton, J. A., Tilgner, A., Williams, B. J., and Zaveri, R. A.: Nitrate radicals and biogenic volatile organic compounds: oxidation, mechanisms, and organic aerosol, *Atmospheric Chemistry and Physics*, 17, 2103–2162, <https://doi.org/10.5194/acp-17-2103-2017>, 2017.
- 630 Orlando, J. J. and Tyndall, G. S.: Laboratory studies of organic peroxy radical chemistry: an overview with emphasis on recent issues of atmospheric significance, *Chem. Soc. Rev.*, 41, 6294–6317, <https://doi.org/10.1039/C2CS35166H>, 2012.
- 635 Palm, B. B., Campuzano-Jost, P., Ortega, A. M., Day, D. A., Kaser, L., Jud, W., Karl, T., Hansel, A., Hunter, J. F., Cross, E. S., Kroll, J. H., Peng, Z., Brune, W. H., and Jimenez, J. L.: In situ secondary organic aerosol formation from ambient pine forest air using an oxidation flow reactor, *Atmospheric Chemistry and Physics*, 16, 2943–2970, 2016.
- Park, J. Y. and Lee, Y. N.: Solubility and decomposition kinetics of nitrous acid in aqueous solution, *J. Phys. Chem.*, 92, 6294–6302, <https://doi.org/10.1021/j100333a025>, 1988.
- 640 Peng, Z. and Jimenez, J. L.: KinSim: A Research-Grade, User-Friendly, Visual Kinetics Simulator for Chemical-Kinetics and Environmental-Chemistry Teaching, *J. Chem. Educ.*, 96, 806–811, <https://doi.org/10.1021/acs.jchemed.9b00033>, 2019.
- Poskrebyshev, G. A., Neta, P., and Huie, R. E.: Equilibrium constant of the reaction $\cdot\text{OH} + \text{HNO}_3 \rightleftharpoons \text{H}_2\text{O} + \text{NO}_3$ in aqueous solution, *Journal of Geophysical Research: Atmospheres*, 106, 4995–5004, <https://doi.org/https://doi.org/10.1029/2000JD900702>, 2001.
- Sander, S., Abbatt, J. P. D., Barker, J. R., Burkholder, J. B., Friedl, R. R., Golden, D. M., Huie, R. E., Kolb, C. E., Kurylo, M. J., Moortgat, G. K., Orkin, V. L., and Wine, P. H.: Chemical Kinetics and Photochemical Data for Use in Atmospheric Studies, Evaluation Number 17, JPL Publication 10-6, 2011.
- 645 Sander, S. P.: Temperature dependence of the nitrogen trioxide absorption spectrum, *J. Phys. Chem.*, 90, 4135–4142, 1986.
- Sauer, M. C. J., Brown, W. G., and Hart, E. J.: Oxygen(3P) atom formation by the photolysis of hydrogen peroxide in alkaline aqueous solutions, *J. Phys. Chem.*, 88, 1398–1400, <https://doi.org/10.1021/j150651a033>, 1984.

- 650 Saunders, S., Jenkin, M., Derwent, R., and Pilling, M.: Protocol for the development of the Master Chemical Mechanism, MCM v3 (Part A): tropospheric degradation of non-aromatic volatile organic compounds, *Atmospheric Chemistry and Physics*, 3, 161–180, 2003.
- Schott, G. and Davidson, N.: Shock Waves in Chemical Kinetics: The Decomposition of N₂O₅ at High Temperatures¹, *J. Am. Chem. Soc.*, 80, 1841–1853, <https://doi.org/10.1021/ja01541a019>, 1958.
- Schwab, J. J., Brune, W. H., and Anderson, J. G.: Kinetics and mechanism of the hydroxyl + hydroperoxo reaction, *J. Phys. Chem.*, 93, 655 1030–1035, <https://doi.org/10.1021/j100340a005>, 1989.
- Shen, H., Zhao, D., Pullinen, I., Kang, S., Vereecken, L., Fuchs, H., Acir, I.-H., Tillmann, R., Rohrer, F., Wildt, J., Kiendler-Scharr, A., Wahner, A., and Mentel, T. F.: Highly Oxygenated Organic Nitrates Formed from NO₃ Radical-Initiated Oxidation of β -Pinene, *Environ. Sci. Technol.*, 55, 15 658–15 671, <https://doi.org/10.1021/acs.est.1c03978>, 2021.
- Stockwell, W. R. and Calvert, J. G.: The near ultraviolet absorption spectrum of gaseous HONO and N₂O₃, *Journal of Photochemistry*, 8, 660 193–203, [https://doi.org/https://doi.org/10.1016/0047-2670\(78\)80019-7](https://doi.org/https://doi.org/10.1016/0047-2670(78)80019-7), 1978.
- Strehlow, H. and Wagner, I.: Flash Photolysis in Aqueous Nitrite Solutions, *Zeitschrift für Physikalische Chemie*, 132, 151–160, <https://doi.org/doi:10.1524/zpch.1982.132.2.151>, 1982.
- Takeuchi, M. and Ng, N. L.: Chemical composition and hydrolysis of organic nitrate aerosol formed from hydroxyl and nitrate radical oxidation of α -pinene and β -pinene, *Atmospheric Chemistry and Physics*, 19, 12 749–12 766, <https://doi.org/10.5194/acp-19-12749-2019>, 665 2019.
- Veres, P. R., Roberts, J. M., Wild, R. J., Edwards, P. M., Brown, S. S., Bates, T. S., Quinn, P. K., Johnson, J. E., Zamora, R. J., and de Gouw, J.: Peroxynitric acid (HO₂NO₂) measurements during the UBWOS 2013 and 2014 studies using iodide ion chemical ionization mass spectrometry, *Atmospheric Chemistry and Physics*, 15, 8101–8114, <https://doi.org/10.5194/acp-15-8101-2015>, 2015.
- Wagner, N. L., Dubé, W. P., Washenfelder, R. A., Young, C. J., Pollack, I. B., Ryerson, T. B., and Brown, S. S.: Diode laser-based 670 cavity ring-down instrument for NO₃, N₂O₅, NO, NO₂ and O₃ from aircraft, *Atmospheric Measurement Techniques*, 4, 1227–1240, <https://doi.org/10.5194/amt-4-1227-2011>, 2011.
- Wang, H., Wang, H., Lu, X., Lu, K., Zhang, L., Tham, Y. J., Shi, Z., Aikin, K., Fan, S., Brown, S. S., and Zhang, Y.: Increased night-time oxidation over China despite widespread decrease across the globe, *Nature Geoscience*, 16, 217–223, <https://doi.org/10.1038/s41561-022-01122-x>, 2023.
- 675 Wayne, R., Barnes, I., Biggs, P., Burrows, J., Canosa-Mas, C., Hjorth, J., Le Bras, G., Moortgat, G., Perner, D., Poulet, G., Restelli, G., and Sidebottom, H.: The nitrate radical: Physics, chemistry, and the atmosphere, *Atmospheric Environment. Part A. General Topics*, 25, 1–203, [https://doi.org/https://doi.org/10.1016/0960-1686\(91\)90192-A](https://doi.org/https://doi.org/10.1016/0960-1686(91)90192-A), the nitrate radical: Physics, Chemistry, and the Atmosphere, 1991.
- Wine, P. H., Mauldin, R. L., and Thorn, R. P.: Kinetics and spectroscopy of the nitrogen oxide radical (NO₃) in aqueous ceric nitrate-nitric acid solutions, *J. Phys. Chem.*, 92, 1156–1162, <https://doi.org/10.1021/j100316a031>, 1988.
- 680 Wylie, A. W.: Extraction of ceric nitrate by solvents, *J. Chem. Soc.*, pp. 1474–1480, <https://doi.org/10.1039/JR9510001474>, 1951.

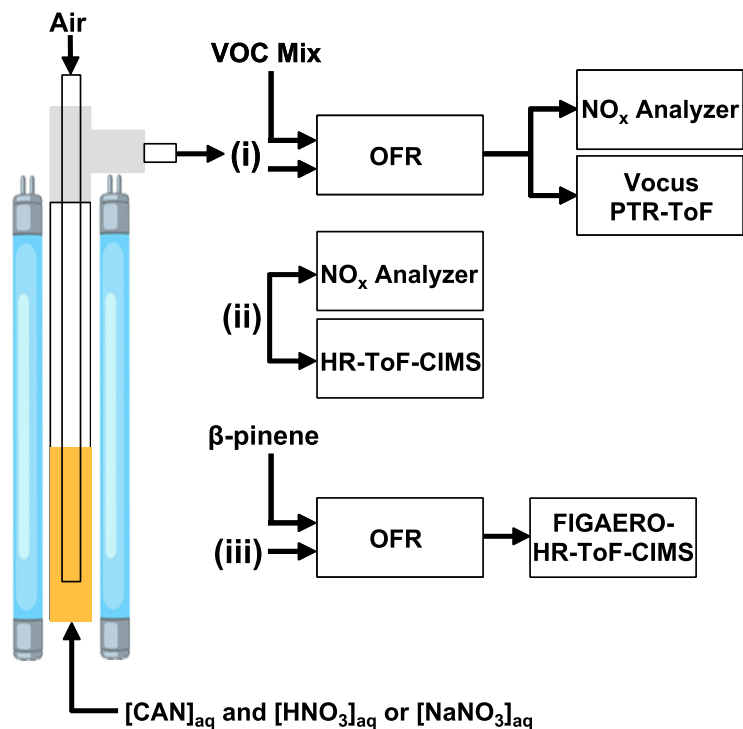


Figure 1. Overview of experiments conducted in this study. Aqueous mixtures of ceric ammonium nitrate (CAN) and nitric acid (HNO₃) or sodium nitrate (NaNO₃) were irradiated in a photoreactor to generate nitrate radicals (NO₃) in solution. Air was bubbled through the solution to evaporate NO₃ and other volatile photolysis products into the gas phase. The photoreactor effluent was then (i) injected into a dark oxidation flow reactor (OFR) along with a VOC mixture to characterize [NO₃] via tracer decay measurements using a Vocus proton transfer-reaction time-of-flight mass spectrometer (PTR-ToF) (ii) sampled with an iodide adduct high-resolution time-of-flight chemical ionization mass spectrometer (HR-ToF-CIMS) (iii) injected into a dark OFR to characterize β-pinene/NO₃ oxidation products with a Filter Inlet for Gases and Aerosols (FIGAERO) coupled to the HR-ToF-CIMS. Supporting measurements were obtained using a NO_x analyzer.

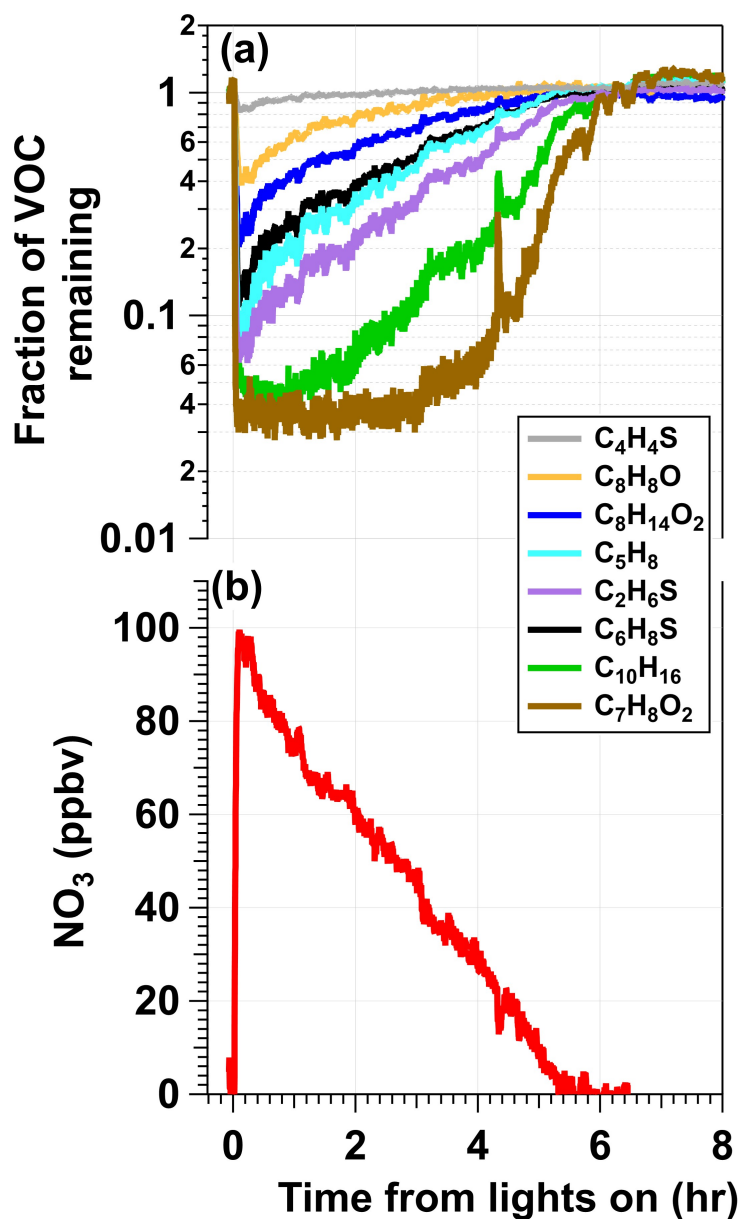


Figure 2. Example results from an experiment in which a mixture of 0.5 M CAN and 6.0 M HNO_3 was irradiated to generate NO_3 ($\lambda_{max} = 369$ nm, $I_{369} = 7 \times 10^{15}$ photons $cm^{-2} s^{-1}$) that was injected into the OFR along with a reactive VOC tracer mixture. **(a)** Time series of the fractional consumption of VOC tracers measured with the Vocus following irradiation: thiophene (C_4H_4S), 2,3-dihydrobenzofuran (C_8H_8O), cis-3-hexenyl-1-acetate ($C_8H_{14}O_2$), isoprene (C_5H_8), dimethyl sulfide (C_2H_6S), 2,5-dimethylthiophene (C_6H_8S), α -pinene ($C_{10}H_{16}$), guaiacol ($C_7H_8O_2$). Signals of each tracer were normalized to their initial concentrations prior to NO_3 exposure and to acetonitrile concentrations to account for changes in the syringe pump output. **(b)** Time series of $[NO_3]$ calculated from **(a)** and Tab. S1.

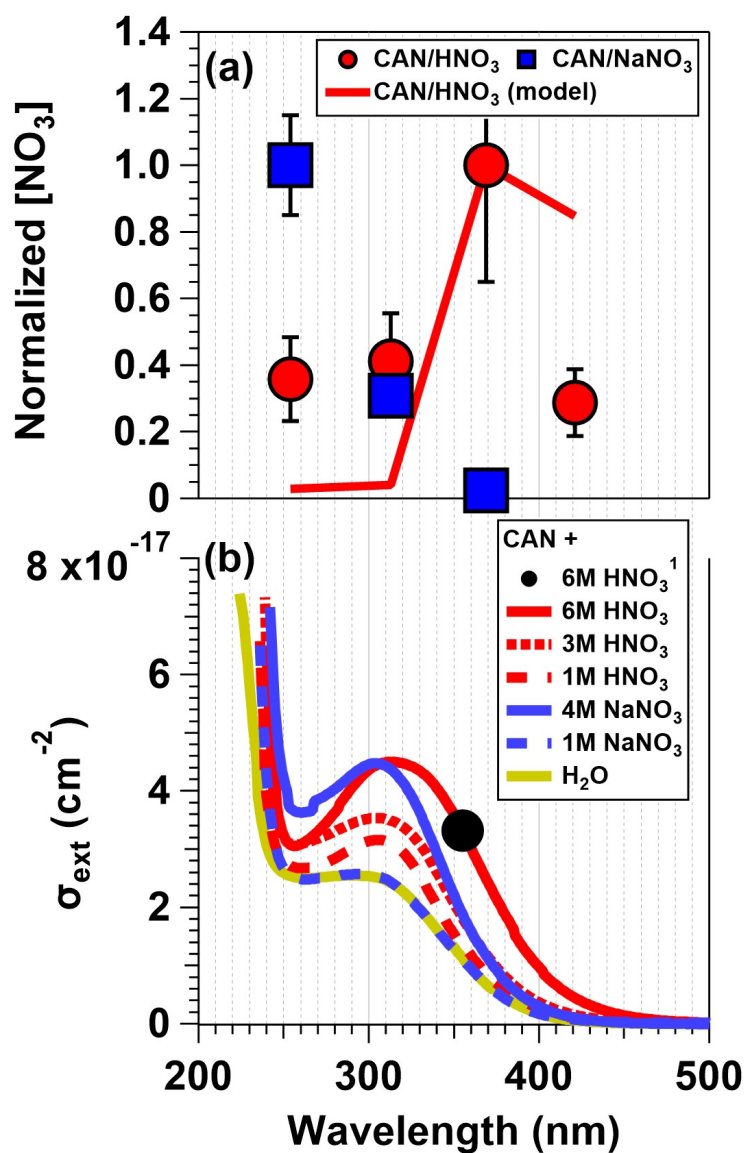


Figure 3. (a) $[\text{NO}_3]$ values obtained from irradiated CAN & 6.0 M HNO_3 and CAN & 4.8 M NaNO_3 mixtures as a function of irradiation wavelength. Results were normalized to $[\text{NO}_3]$ achieved with irradiation of CAN/ HNO_3 mixtures at $\lambda = 369$ nm or CAN/ NaNO_3 mixtures at $\lambda = 254$ nm. Error bars represent $\pm 1\sigma$ uncertainty in binned $[\text{NO}_3]$ values. (b) Extinction cross sections (σ_{ext}) of CAN/ HNO_3 and CAN/ NaNO_3 mixtures (for details see Sect. 2.3). **Additional figure notes:**¹ The black dot corresponds to data from Wine et al. (1988).

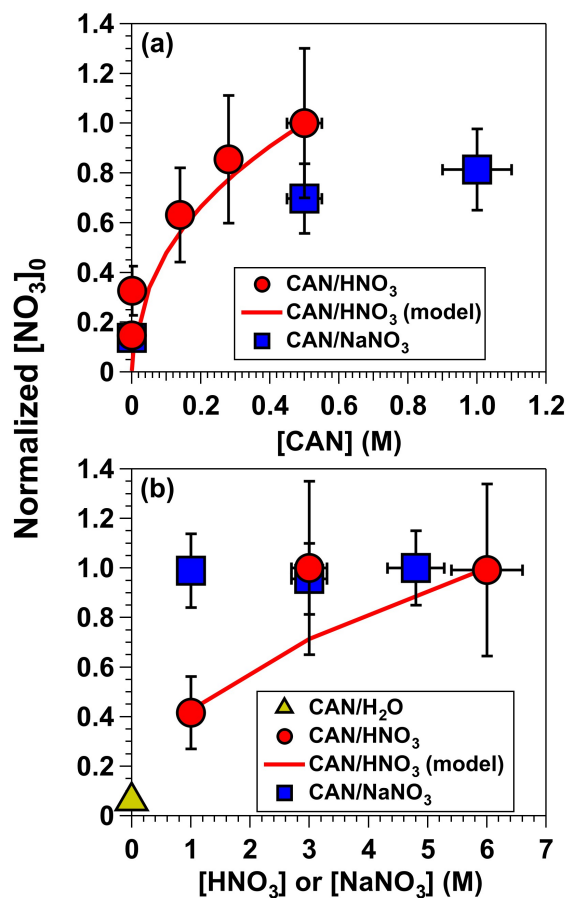


Figure 4. $[\text{NO}_3]$ obtained from (a) irradiated 6.0 M HNO_3 solutions containing 0.001 to 0.5 M CAN ($I_{369} = 7 \times 10^{15}$ photons $\text{cm}^{-2} \text{s}^{-1}$), and irradiated 1.0 M NaNO_3 solutions containing 0.5 to 1.0 M CAN ($I_{254} = 1 \times 10^{16}$ photons $\text{cm}^{-2} \text{s}^{-1}$). (b) irradiated 0.5 M CAN solutions containing 1.0 to 6.0 M $[\text{HNO}_3]$ or 1.0 to 4.8 M $[\text{NaNO}_3]$ at the same I_{369} and I_{254} values used to obtain results shown in (a). Results were normalized to $[\text{NO}_3]$ achieved with mixtures of 0.5 M CAN and 6.0 M HNO_3 . Error bars represent estimated $\pm 35\%$ uncertainty in $[\text{NO}_3]$ values obtained from CAN/HNO_3 mixtures, $\pm 15\%$ uncertainty in $[\text{NO}_3]$ values obtained from CAN/NaNO_3 mixtures, and $\pm 10\%$ uncertainty in $[\text{CAN}]$, $[\text{HNO}_3]$, and $[\text{NaNO}_3]$ values.

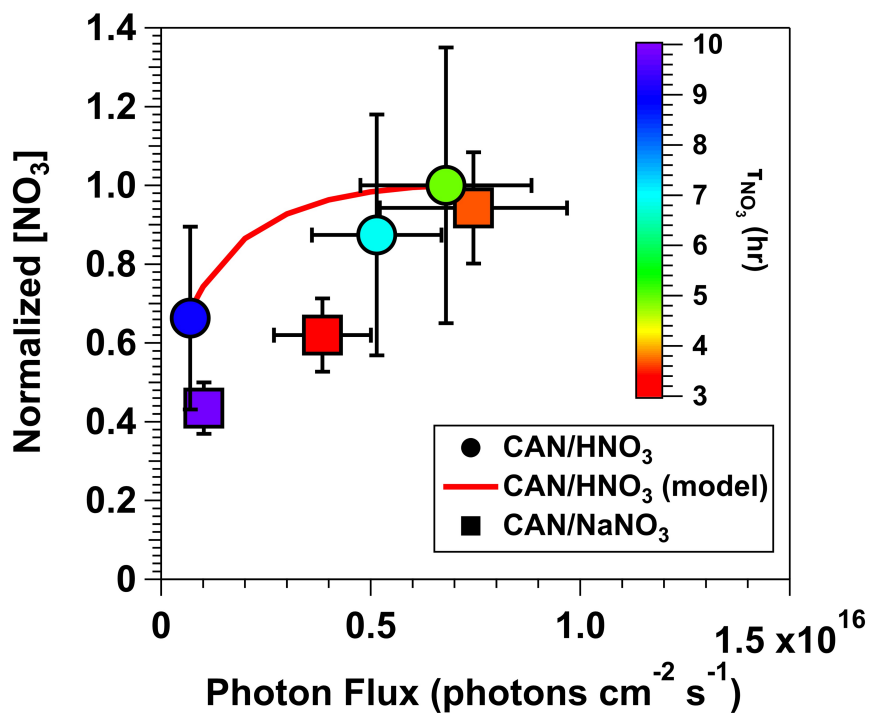


Figure 5. Normalized $[\text{NO}_3]$ values obtained from irradiated mixtures of 0.5 M CAN and 6.0 M HNO_3 ($\lambda = 369 \text{ nm}$) or 0.5 M CAN and 1.0 M NaNO_3 ($\lambda = 254 \text{ nm}$) as a function of photon flux ranging from 6.9×10^{14} to 7.5×10^{15} photons $\text{cm}^{-2} \text{ s}^{-1}$. Results were normalized to $[\text{NO}_3]$ achieved with 0.5 M CAN, 6.0 M HNO_3 and $I_{369} = 6.8 \times 10^{15}$ photons $\text{cm}^{-2} \text{ s}^{-1}$. Symbols are colored by the time it took for $[\text{NO}_3]$ to experience one e-fold decay relative to the maximum $[\text{NO}_3]$ that was measured (τ_{NO_3}). Error bars represent estimated $\pm 35\%$ uncertainty in $[\text{NO}_3]$ values obtained from CAN/ HNO_3 mixtures, $\pm 15\%$ uncertainty in $[\text{NO}_3]$ values obtained from CAN/ NaNO_3 mixtures, and $\pm 30\%$ uncertainty in photon flux values.

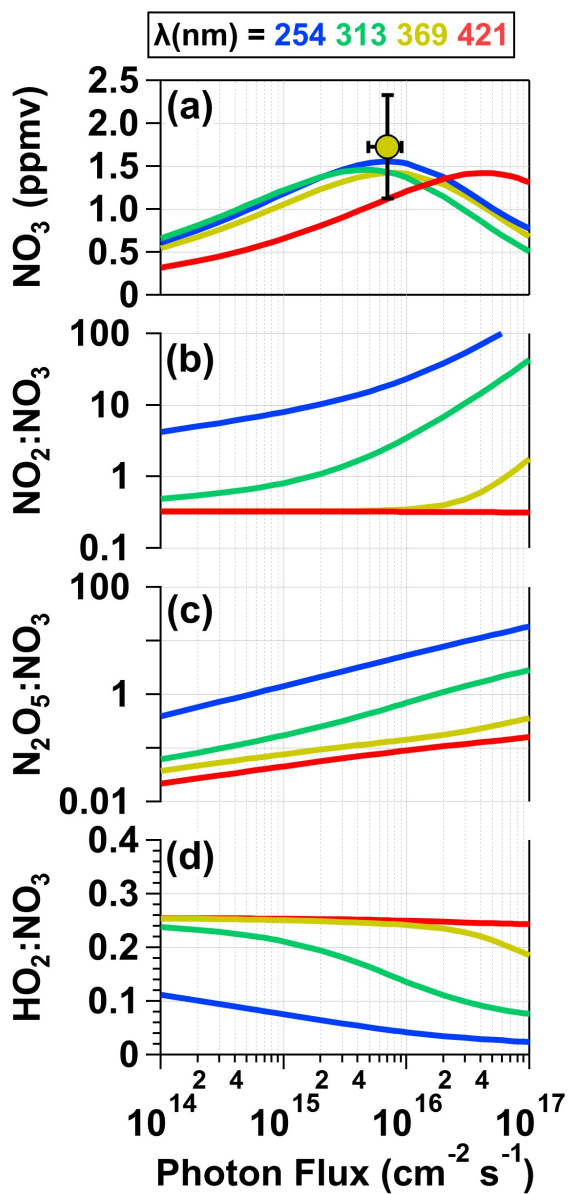


Figure 6. Model-calculated (a) $[\text{NO}_3]$, (b) $\text{NO}_2:\text{NO}_3$, (c) $\text{HO}_2:\text{NO}_3$, and (d) $\text{N}_2\text{O}_5:\text{NO}_3$ values in solution as a function of photon flux ranging from 1×10^{14} to 1×10^{17} photons $\text{cm}^{-2} \text{s}^{-1}$ following $\lambda = 254, 313, 369$ and 421 nm irradiation of a mixture containing 0.5 M CAN and 6.0 M HNO_3 . $[\text{NO}_3]$ obtained from measurements shown in Fig. 2 is plotted in (a). For details see Sect. 2.3 and Tab. S2.

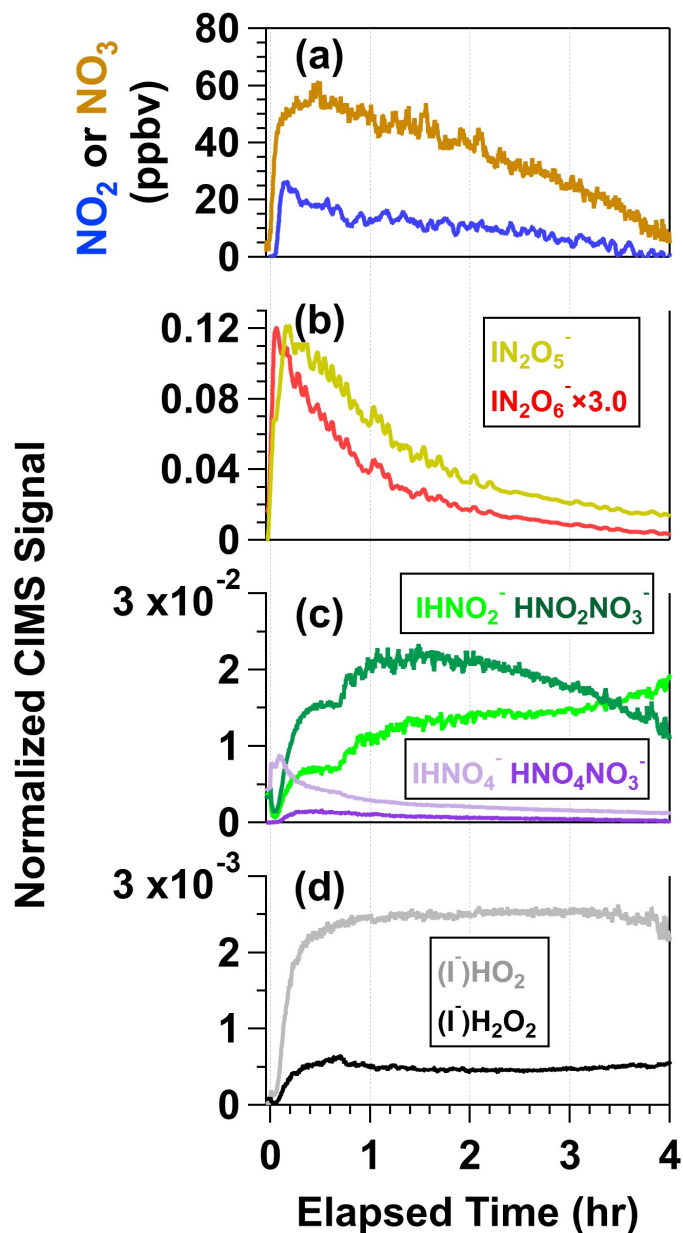


Figure 7. Time series of **a** (a) NO_2 and NO_3 , (b) N_2O_5 and N_2O_6 , (c) HNO_2 and HNO_4 , and (d) HO_2 and H_2O_2 detected following irradiation of a mixture containing 0.5 M CAN and 1.0 M NaNO_3 . N_2O_5 , N_2O_6 , HO_2 and H_2O_2 were detected as I^- adducts, and HNO_2 and HNO_4 were detected as both I^- and NO_3^- adducts with HR-ToF-CIMS. CIMS signals detected as iodide adducts were normalized to the I^- signal prior to the start of the experiment, and CIMS signals detected as nitrate adducts were normalized to the maximum NO_3^- obtained during the experiment (see Fig. S5).

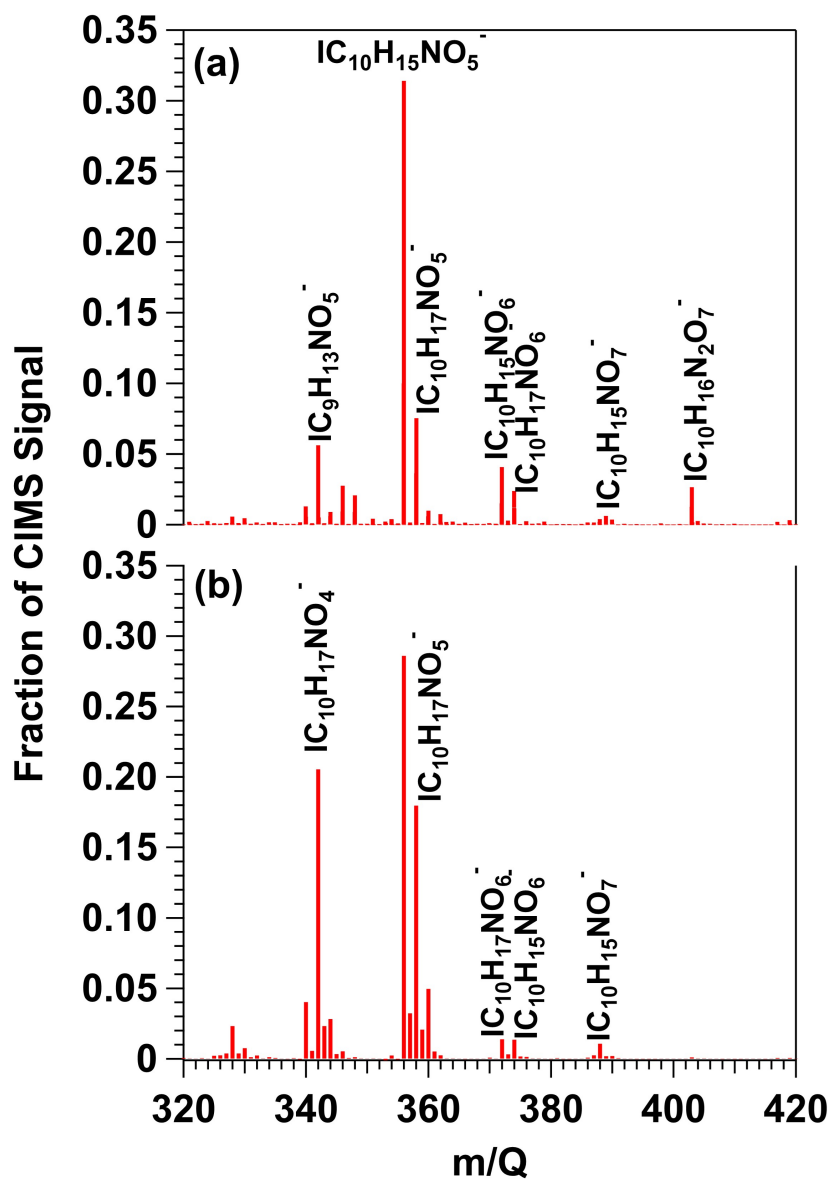


Figure 8. HR-ToF-CIMS spectra of gas-phase β -pinene/ NO_3 oxidation products obtained following β -pinene reaction with NO_3 generated via (a) irradiation of a mixture of 0.5 M CAN and 3.0 M HNO_3 and subsequent injection into the OFR (b) thermal decomposition of N_2O_5 injected into the Georgia Tech environmental chamber. Signals shown are unmodified $(\text{M}+\text{I})^-$ formulas.

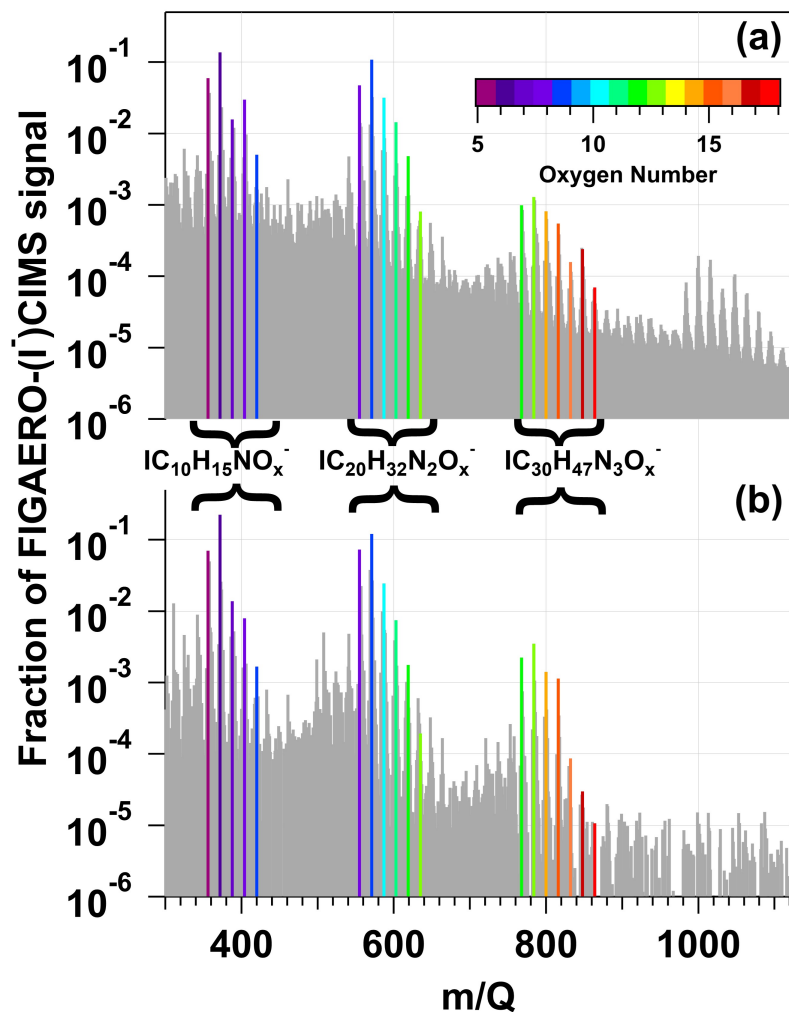


Figure 9. FIGAERO-HR-ToF-CIMS spectra of condensed-phase β -pinene/ NO_3 oxidation products obtained following β -pinene reaction with NO_3 generated via (a) irradiation of a mixture of 0.5 M CAN and 3.0 M HNO_3 and subsequent injection into an OFR (b) thermal decomposition of N_2O_5 injected into the Georgia Tech environmental chamber. Signals shown are unmodified $(M+I)^-$ formulas. Bands of ion signals corresponding to $C_{10}H_{15}NO_x$, $C_{20}H_{32}N_2O_x$, and $C_{30}H_{47}N_3O_x$ oxidation products are highlighted and colored by the number of oxygen atoms in their chemical formulas.

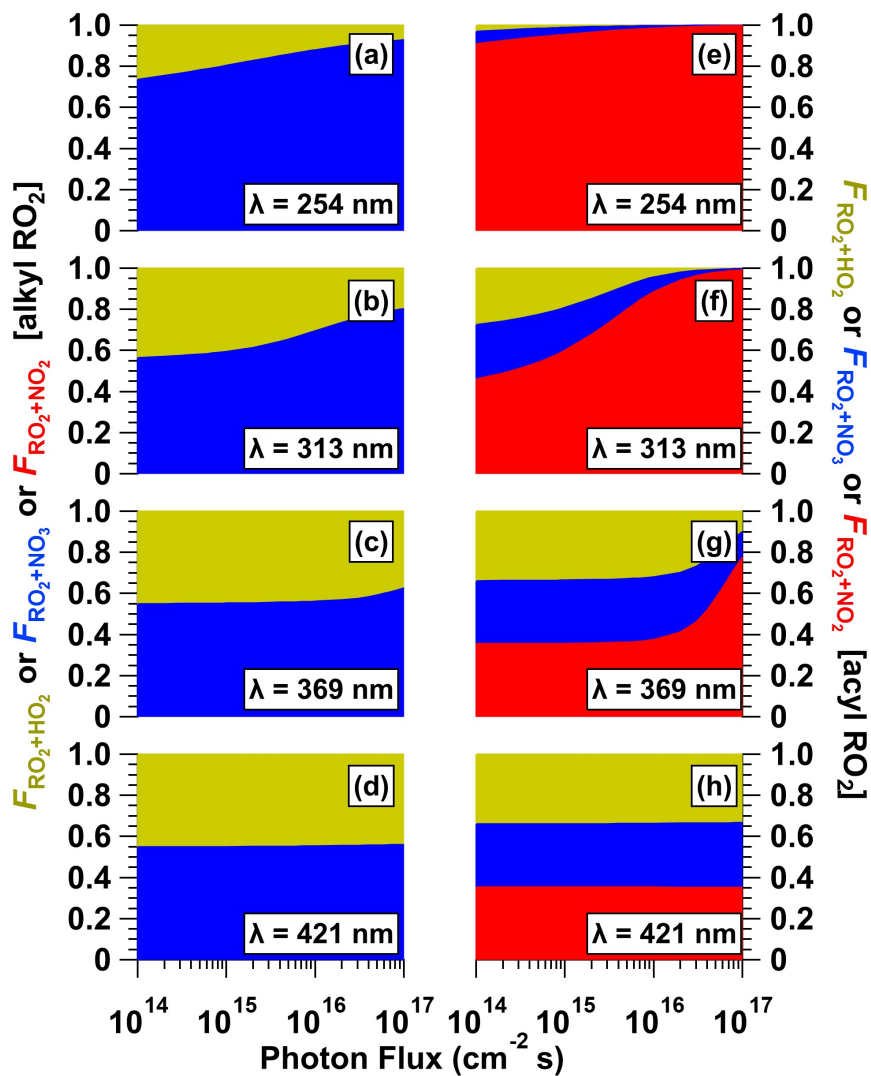


Figure 10. Fractional oxidative loss of alkyl and acyl organic peroxy radicals (RO_2) due to reaction with HO_2 , NO_3 and NO_2 ($F_{\text{RO}_2+\text{HO}_2}$, $F_{\text{RO}_2+\text{NO}_3}$ and $F_{\text{RO}_2+\text{NO}_2}$) generated following $\lambda =$ (a), (e) 254 (b), (f) 313 (c), (g) 369 (d), (h) 421 nm irradiation of a mixture containing 0.5 M CAN and 6.0 M HNO_3 as a function of photon flux ranging from 1×10^{14} to 1×10^{17} photons $\text{cm}^{-2} \text{s}^{-1}$.